

# The impact of bars on the mid-infrared dust emission of spiral galaxies: global and circumnuclear properties\*

H. Roussel<sup>1</sup>, M. Sauvage<sup>1</sup>, L. Vigroux<sup>1</sup>, A. Bosma<sup>2</sup>, C. Bonoli<sup>3</sup>,  
P. Gallais<sup>1</sup>, T. Hawarden<sup>4</sup>, S. Madden<sup>1</sup>, and P. Mazzei<sup>3</sup>

<sup>1</sup> DAPNIA/Service d'Astrophysique, CEA/Saclay, 91191 Gif-sur-Yvette cedex, France

<sup>2</sup> Observatoire de Marseille, 2 Place Le Verrier, 13248 Marseille cedex 4, France

<sup>3</sup> Osservatorio Astronomico di Padova, 5 Vicolo dell'Osservatorio, 35122 Padova, Italy

<sup>4</sup> Joint Astronomy Center, 660 N. A'ohoku Place, Hilo, Hawaii 96720, USA

Received / accepted

**Abstract.** We study the mid-infrared properties of a sample of 69 nearby spiral galaxies, selected to avoid Seyfert activity contributing a significant fraction of the central energetics, or strong tidal interaction, and to have normal infrared luminosities. These observations were obtained with ISOCAM, which provides an angular resolution of the order of  $10''$  (half-power diameter of the point spread function) and low-resolution spectro-imaging information. Between  $5$  and  $18\mu\text{m}$ , we mainly observe two dust phases, aromatic infrared bands and very small grains, both out of thermal equilibrium. On this sample, we show that the global  $F_{15}/F_7$  colors of galaxies are very uniform, the only increase being found in early-type strongly barred galaxies, consistent with previous IRAS studies. The  $F_{15}/F_7$  excesses are unambiguously due to galactic central regions where bar-induced starbursts occur. However, the existence of strongly barred early-type galaxies with normal circumnuclear colors indicates that the relationship between a distortion of the gravitational potential and a central starburst is not straightforward.

As the physical processes at work in central regions are in principle identical in barred and unbarred galaxies, and since this is where the mid-infrared activity is mainly located, we investigate the mid-infrared circumnuclear properties of all the galaxies in our sample. We show how surface brightnesses and colors are related to both the available molecular gas content and the mean age of stellar populations contributing to dust heating. Therefore, the star formation history in galactic central regions can be constrained by their position in a color-surface brightness mid-infrared diagram.

**Key words:** galaxies: spiral – galaxies: barred – galaxies: ISM – stars: formation – infrared: ISM: continuum – infrared: ISM: lines and bands

## 1. Introduction

As the high frequency of bars in galaxies becomes more evident (*e.g.* Eskridge et al. 2000), and as new techniques emerge to both observationally quantify their strength (Seigar & James 1998; Buta & Block 2000) and numerically simulate them, their effects on their host galaxies are of major interest, and in particular, it is worth checking whether they are indeed very efficient systems to drive nuclear starbursts in spiral galaxies.

Numerous studies have dealt with the respective star formation properties of barred and non-barred spirals, mostly in the infrared, since this is the wavelength regime where starbursts are expected to be most easily detectable. Yet conclusions derived from such studies appear to contradict each other, partly because the different selection criteria result in samples with a more or less pronounced bias toward starburst objects. For instance, in the IR-bright sample analyzed by Hawarden et al. (1986), an important fraction of SB and SAB galaxies (respectively strongly barred and weakly barred spirals in the classification of de Vaucouleurs et al. 1991) shows a  $25\mu\text{m}$  emission excess (with respect to  $12$  and  $100\mu\text{m}$ ) absent in the SA subsample (non-barred spirals), which can be accounted for by a highly increased contribution of Galactic-like HII regions to the total emission. On the other hand, Isobe & Feigelson (1992), using a volume-limited sample and performing a survival analysis to take into account the frequent IRAS non-detections, found that the far-IR to blue flux ratio ( $F_{\text{FIR}}/F_B$ ) is rather independent of the bar class. The contradiction is marginal since  $F_{\text{FIR}}/F_B$  does not give a direct estimation of the star formation activity, especially when dealing with quiescent normal galaxies: the blue light originates partly from young stars and, as

Send offprint requests to: H. Roussel (e-mail: hroussel@cea.fr)

\* Based on observations with ISO, an ESA project with instruments funded by ESA Member States (especially the PI countries: France, Germany, the Netherlands and the United Kingdom) and with the participation of ISAS and NASA.

Isobe & Feigelson (1992) emphasize,  $F_{\text{FIR}}/F_B$  depends on the amount and spatial distribution of dust with respect to stars. The relationship between the  $25\text{ }\mu\text{m}$  excess, quantified by  $F_{25}/F_{12}$ , and  $F_{\text{FIR}}/F_B$  in a galaxy sample with good quality data is indeed highly dispersed. Huang et al. (1996) investigated the  $25\text{ }\mu\text{m}$  excess as a function of IR brightness and reconciled the two previous analyzes: a significant excess can occur only if  $F_{\text{FIR}}/F_B$  is larger than a threshold value of  $\simeq 0.3$ . Therefore, a statistical effect of bars on star formation can be demonstrated only in suitably selected samples. Huang et al. (1996) also emphasized that the difference between barred and unbarred spirals concerns only early types (S0/a to Sbc).

Studies of the infrared excess in barred galaxies mostly rest on the integrated IRAS measurements, which do not allow the determination of the nature and location of regions responsible for this excess. However, dynamical models and observations at other wavelengths give evidence that the infrared activity should be concentrated in circumnuclear regions (see for instance the study of NGC 5383 by Sheth et al. 1999). In addition, high-resolution ground-based observations near  $10\text{ }\mu\text{m}$  of galaxy centers (Devereux 1987; Telesco et al. 1993) have shown that the dust emission is more concentrated in barred galaxies.

Theoretically, bars are known to be responsible for large-scale redistribution of gas through galactic disks. In a strong barred perturbation of the gravitational potential, shocks develop along the rotation-leading side of the bar and are associated with strong shear, as shown by Athanassoula (1992) and references therein (also Friedli & Benz 1993). They induce an increase of gas density which is traced by the thin dust lanes widely observed in bars, producing a contrasting absorption of optical light (Prendergast 1962, unpublished; Huntley et al. 1978). Due to these shocks, gas loses angular momentum and flows towards the circumnuclear region. This picture is confirmed by direct observations of inward velocity gradients across bars in ionized gas lines, CO and H $\text{I}$  (e.g. Lindblad et al. 1996; Reynaud & Downes 1998; Mundell & Shone 1999). Regan et al. (1997) derive a gas accretion rate of  $\approx 1\text{ M}_\odot\text{ yr}^{-1}$  into the circumnuclear ring of NGC 1530.

Statistical evidence is also found for higher gas concentrations in the center of barred galaxies (Sakamoto et al. 1999, who however observed only SABs, except NGC 1530), and for more frequent circumnuclear starbursts in barred galaxies, as reported by Heckman (1980), Hawarden et al. (1986), Arsenault (1989) (who, more exactly, found more probable starbursts in galaxies with both bar and inner ring, supposed to be a signature of one or two inner Lindblad resonance(s)), Huang et al. (1996), Martinet & Friedli (1997) and Bonatto et al. (1998). Aguerri (1999) has moreover reported that the global star formation intensity of isolated spirals (mostly of late types) is correlated with bar strength as quantified by means of its projected axial ratio, which is surpris-

ing in view of the very different timescales of bar evolution ( $\approx 1\text{ Gyr}$ ) and star formation in kpc-scale regions ( $\approx 10^{7-8}\text{ yr}$ ). Indeed, Martinet & Friedli (1997), using carefully selected late-type galaxies, found no such correlation, the bar strength being quantified either by its deprojected axis ratio or its deprojected length relative to the disk diameter. The fact that only a fraction of strongly barred galaxies exhibit star formation excess (as evidenced by their IRAS colors) is explained by these authors with numerical simulations of bar evolution including gas physics. They show that a strong starburst occurs shortly after bar formation and quickly fades away (in typically less than 1 Gyr); meanwhile, the strength and other properties of the bar evolve, but the bar remains strong if it was initially strong. The existence of strongly barred galaxies in a quiescent state is thus to be expected, presumably because the available gas supply has been consumed in previous bursts.

This paper is aimed at characterizing the mid-infrared excess in barred galaxies, with the possibility to carry out a detailed and systematic spatial analysis due to the good angular resolution of ISOCAM (the half-power beam diameter is less than  $10''$  at  $7\text{ }\mu\text{m}$ ), and hence to locate unambiguously sites of enhanced infrared activity. Although dust is a more indirect tracer of young stars than far-ultraviolet ionizing radiation or optical recombination lines, the infrared emission suffers relatively minor extinction effects, which are very difficult to correct and hamper shorter wavelength studies. In a companion paper (Roussel et al. 2001a, hereafter Paper II), we have shown that in galactic disks, mid-infrared emission is a reliable star formation indicator. Here, we concentrate on central regions of galaxies where the dust heating regime is markedly different from that in disks.

For this purpose, we have analyzed a sample of 69 nearby spiral galaxies, imaged at  $7$  and  $15\text{ }\mu\text{m}$  with the camera ISOCAM on board ISO (described by Cesarsky et al. 1996c). We have also obtained low-resolution spectroscopic information for a few galaxies, enabling us to identify and separate the various dust components emitting between  $5$  and  $18\text{ }\mu\text{m}$ .  $7\text{ }\mu\text{m}$  images and  $F_{15}/F_7$  flux density ratios of selected regions, together with optical images, are presented in Roussel et al. (2001b) (hereafter the Atlas). For a description of data reduction and analysis, and a summary of morphological properties of the sample, the reader is also referred to the Atlas.

## 2. The galaxy sample

The sample is intended to be representative of normal quiescent spirals, and contains galaxies of moderate infrared luminosity. It covers three guaranteed time programs of ISOCAM. The first one (*Cambarre*) consists of nearby barred galaxies, the second one (*Camspir*) of a few large-size spirals of special interest (NGC 1365, 4736, 5194, 5236, 5457 and 6744) and another subsample is

drawn from the Virgo cluster sample of Boselli et al. (1998) (*Virgo* program), containing relatively fainter and smaller galaxies, both barred and unbarred. This sample was supplemented by comparable spirals in the ISOCAM public archive, from the programs *Sf\_glx* (Dale et al. 2000) and *Irgal* (PI T. Onaka). All of the observations were reduced in the same way to form a homogeneous sample. The final set comprises 69 spiral galaxies at distances between 4 and 60 Mpc. We have divided them into three main categories according to morphological classes in the RC3 (de Vaucouleurs et al. 1991): SBs (accounting for about half the sample with 37 galaxies), SABs (20 galaxies) and SAs (12 galaxies). The latter two classes are merged to form the control sample to compare with SB galaxies. This sample, although not statistically complete, has been selected according to the following requirements:

- All objects are relatively nearby, which ensures good spatial resolution with a 6" or 3" pixel size (the extension of the central concentration is typically 5–10 pixels in diameter). At the distances of the sample, a 3" pixel corresponds to linear sizes between 60 and 900 pc. Virgo galaxies, less extended and all imaged with 6" pixels in order to increase the signal to noise ratio, are resolved but with less detail.
- The sample was selected to avoid non-stellar activity as well as strong signs of tidal interaction, with a few exceptions in the *Cambarre* and *Virgo* subsamples, detailed in the following.
- Galaxies included in the first two programs are moderately inclined on the line of sight ( $i \leq 50^\circ$ ). This was not a requirement for the other programs, so that one third of the Virgo galaxies and one third of the supplementary galaxies are inclined by more than 60°.
- The number of SA-SAB galaxies is comparable to that of SBs and both groups span the whole de Vaucouleurs spiral sequence from types S0/a to Sdm.
- Both barred and unbarred galaxies cover a large range of far-infrared luminosities (between  $10^{8.6}$  and  $10^{11} L_{\odot\text{bol}}$ ), but none would be classified as an infrared luminous galaxy, except NGC 7771 which is at the lower boundary of this class – defined by  $10^{11} < L_{\text{FIR}} < 10^{12} L_{\odot\text{bol}}$  (Sanders & Mirabel 1996).

Another property which was not a selection criterion is that absolute blue magnitudes are equal to or greater than the typical magnitude of the Schechter luminosity function in the field,  $M_B^* \simeq -21$  (more exactly, they range between -21.17 and -17.38).

Despite the incompleteness of the sample, we have checked that it is very similar to the magnitude-limited CfA galaxy sample (Thuan & Sauvage 1992), from the point of view of its infrared brightness normalized by blue starlight. For CfA spiral galaxies detected in all 4 IRAS bands and with blue magnitudes in the RC3,  $\log(F_{\text{FIR}}/F_B)$  falls in the interval  $[-0.97; +0.98]$  with a mean value of 0.05. Using the same IRAS references as

those in Thuan & Sauvage (1992), *i.e.* by order of preference Thuan & Sauvage (1992), Rice et al. (1988), Soifer et al. (1989) and Moshir et al. (1989), galaxies in our sample have  $\log(F_{\text{FIR}}/F_B)$  in the interval  $[-1.58; +1.67]$  with a mean value of 0.01. For that set of references, a Wilcoxon-Mann-Whitney (WMW) test indicates that the probability for the two populations to have the same  $F_{\text{FIR}}/F_B$  distribution is about 75%. We note that the IRAS 12  $\mu\text{m}$  fluxes often disagree with our 7 and 15  $\mu\text{m}$  fluxes, although the bandpasses overlap. Thus, when we use IRAS data, we take them from the references we consider the most reliable (*i.e.* which provide the best match between 12  $\mu\text{m}$  and our 7–15  $\mu\text{m}$  flux densities). In that case,  $\log(F_{\text{FIR}}/F_B)$  falls in the interval  $[-0.77; +0.95]$  with a mean value of 0.02, and the WMW test gives a probability of about 40%. Hence, our sample is not different from optically complete samples regarding the fraction of the energy radiated in the infrared.

Table 1 lists some general characteristics of the galaxies. The morphological classification adopted is that of the RC3 (de Vaucouleurs et al. 1991). Although it is based on blue images, which may not be as appropriate as near-infrared images for detecting bars, many more galaxies are classified as barred in this catalog than for instance in Sandage & Bedke (1994). We have found only two galaxies classified as SA in the RC3 and possessing a bar (as described in the following). A drawback of using the SB and SAB classes of the RC3 is that they do not constitute a measure of the bar dynamical strength. The bar strength is however difficult to quantify, and reliable measures, such as those of Buta & Block (2000), are scarce. In the following, we will refer to bar lengths, normalized by the disk diameter, because longer bars are able to collect gas from inside a larger area and have low axis ratios, which are among the (unsatisfactory) quantities used to estimate bar strengths; bar lengths are in addition relatively easy to measure.

The two sub-samples of spirals found in the field or loose groups and Virgo galaxies have been separated, because they differ both in their aspect in the infrared (Virgo members are fainter and less extended) and in their environment. Although Virgo is not a very rich cluster, the interaction of central galaxies with the intracluster gas and with their neighbours is likely to cause either a depletion or an enhancement of star formation activity in the outer parts of disks and also to have global dynamical consequences. An extreme case is the galaxy NGC 4438 (= VCC 1043), whose very perturbed morphological appearance was successfully modelled by Combes et al. (1988) as the result of a collision with NGC 4435. Several Virgo members have truncated H $\text{i}$  disks due to the interaction with the cluster hot gas (Cayatte et al. 1990); a very clear example is NGC 4569 (= VCC 1690), which on optical photographs shows the juxtaposition of a bright and patchy inner disk structured by star formation sites and dust lanes, and a low surface brightness and

very smooth outer disk with faint spiral arms. Severely  $\text{H}\alpha$ -stripped galaxies can indeed be recognized in the optical as anemic (defined by van den Bergh 1976 as an intermediate and parallel sequence between lenticulars and spirals), due to the suppression of star formation where the gas density is too low. Table 1 also indicates whether signatures of nuclear activity or tidal interaction exist.

In addition to these, some galaxies deserve special comments (see the Atlas for more details) and should be considered cautiously in the interpretation of the data set:

- NGC 337, 1385 and 4027 are strongly asymmetric and fit in the category of magellanic barred spirals.
- NGC 4691 and 1022 have an amorphous structure and highly centrally concentrated interstellar tracers. Their morphology is suggestive of merger results. Their star formation activity may therefore not be a consequence of the bar, since the latter was likely produced at the same time by the same cause, *i.e.* the merger.

### 3. Observations and photometric results

All galaxies were observed with two broadband filters, LW3 (12–18  $\mu\text{m}$ ) and LW2 (5–8.5  $\mu\text{m}$ ), that we shall hereafter designate by their central wavelength, respectively 15 and 7  $\mu\text{m}$ . This was expected to provide  $F_{15}/F_7$  colors directly linked with star formation intensity, since the LW2 filter covers the emission from a family of bands (see Sect. 4), which are ubiquitous in the interstellar medium, and LW3 was supposed to cover mainly a thermal continuum observed to rise faster than the emission bands in star-forming regions, for instance from the IRAS  $F_{25}/F_{12}$  ratio (Helou 1986); however, we will see that the picture is more complicated. Maps covering the whole infrared-emitting disk were constructed in raster mode. In all cases, the field of view is large enough to obtain a reliable determination of the background level, except for NGC 4736 and 6744. The pixel size is either 3" or 6", depending on the galaxy size. The half-power/half-maximum diameters of the point spread function are respectively 6.8"/ $\simeq$  3.1" at 7  $\mu\text{m}$  with a 3" pixel size, 9.5"/5.7" at 7  $\mu\text{m}$  with a 6" pixel size, 9.6"/3.5" at 15  $\mu\text{m}$  with a 3" pixel size and 14.2"/6.1" at 15  $\mu\text{m}$  with a 6" pixel size. The data reduction is described in the Atlas.

Since the emission from various dust species and atomic lines is mixed in the broadband filters (see Sect. 4), it is essential to complement our maps with spectro-imaging data. These allow an estimate of the relative importance of all species as a function of the location inside a galaxy. We have thus obtained spectra between 5 and 16  $\mu\text{m}$  of the inner disks (3'  $\times$  3' or 1.5'  $\times$  1.5') of five bright galaxies: NGC 613, 1097, 1365, 5194 and 5236 (Fig. 1). Spectra averaged over a few central pixels covering approximately the extent of the circumnuclear region (left column) are compared with spectra averaged over the inner disk, excluding the central part and a possible

ghost image (middle column). The right column shows the observed spectrum of the faintest pixels, consisting of the zodiacal spectrum contaminated by emission features from the target galaxy, because the field of view never extends beyond the galactic disk. For this reason, we cannot measure exactly the level of the zodiacal foreground to remove. Instead, as explained in the Atlas, we first fit a reference zodiacal spectrum to the average spectrum of the faintest pixels (excluding the spectral regions where emission features appear). The upper limit to the zodiacal foreground is set by offsetting the fitted spectrum within the dispersion range, with the additional constraint that the corrected disk spectrum remains positive; the lower limit is symmetric to the upper limit with respect to the fit. This makes little difference for the nuclear spectra but it does for the disk spectra, although it does not affect the spectral shape. Note that due to the configuration of the instrument, two different filters are used for the short and long wavelength parts of the spectra, and that a small offset can result at the junction of these filters, around 9.2  $\mu\text{m}$ .

The mid-infrared maps generally show an intense circumnuclear source. Decomposing surface brightness profiles into a central condensation and a disk (see details in the Atlas), we define a radius for this circumnuclear region,  $R_{\text{CNR}}$ . Total fluxes and fluxes inside  $R_{\text{CNR}}$  are listed in Table 2 with the background level for each broadband filter. Explanations about the method employed for photometry and the estimation and meaning of errors can be found in the Atlas. The dominant uncertainty arises from memory effects for relatively bright galaxies, and from other sources of error (essentially the readout and photon noise) for faint galaxies, especially at 15  $\mu\text{m}$ . For galaxies drawn from the *Sf-glx* project, the number of exposures per sky position is very small ( $\simeq 10$ ) and does not allow a proper estimate of memory effects: their photometric errors are thus especially ill-determined. Typical errors are  $\approx 10\%$  at 7  $\mu\text{m}$  and 18% at 15  $\mu\text{m}$ . Note that flux density calibration uncertainties, which are of the order of 5 to 10%, are not included. However, this is a systematic effect, hence not affecting relative fluxes.

### 4. Nature of the mid-infrared emitting species

The spectra shown in Fig. 1 are strikingly similar to one another. They contain some features also seen in spectra of reflection nebulae, atomic and molecular envelopes of HII regions, atmospheres of C-rich evolved stars as well as the diffuse interstellar medium. We can thus safely assume that the results obtained on these resolved Galactic objects can be readily extrapolated to the emission of galaxies where individual sources are no longer resolved.

The emission between 5 and 16  $\mu\text{m}$  is dominated by the so-called unidentified infrared bands (UIBs) at 6.2, 7.7, 8.6, 11.3 and 12.7  $\mu\text{m}$ . Our spectra also display weak features which have previously been detected as broad fea-

tures in SWS spectra of starburst objects (Sturm et al. 2000) at *e.g.* 5.3, 5.7, 10.7, 12.0, 13.6, 14.3 and 15.7  $\mu\text{m}^1$ . A 7.0  $\mu\text{m}$  feature can tentatively be identified as an [ArII] line (6.99  $\mu\text{m}$ ) or an H<sub>2</sub> rotational line (6.91  $\mu\text{m}$ ), but our spectral resolution ( $\Delta\lambda/\lambda \approx 40$ ) prevents a more definite identification. We note however that the [ArII] line has been identified in the high-resolution SWS spectra of starburst galaxies (Sturm et al. 2000).

It was originally proposed by Duley & Williams (1981) that UIBs are due to organic functional groups on carbonaceous grains. Léger & Puget (1984) instead favoured vibration modes of C-C and C-H bonds only, in large polycyclic aromatic molecules not in thermal equilibrium with the local radiation field (the so-called PAH model). The constancy of the spectral energy distribution of UIBs, regardless of the radiation field (Sellgren 1984; Uchida et al. 2000), implies an impulsive heating mechanism, where upon absorption of a single UV photon, the carriers undergo a very rapid and large temperature increase and then radiatively cool before the next absorption. Alternative candidates for the UIB carriers are various hydrogenated and oxygenated carbon grains, amorphous but partially ordered at the smallest scale (Borghesi et al. 1987; Sakata et al. 1987; Papoular et al. 1989), much similar to the idea of Duley & Williams (1981). Recent work by Boulanger et al. (1998b) indicates that UIBs are not due to molecules such as PAHs, but more likely to aggregates of several hundred atoms.

In the interstellar medium surrounding the OB association Trapezium (Roche et al. 1989), the Orion bar (Giard et al. 1994) and M17 (Cesarsky et al. 1996a; Tran 1998), these features are detected in the HII region and the molecular cloud front (provided projection effects are minor), but the emission peaks at the photodissociation interface (see also Brooks et al. 2000). UIB carriers are likely destroyed in HII region cores, although the estimation of the critical radiation field necessary to obtain a significant reduction in UIB carrier abundance still remains to be done (*compare e.g.* Boulanger et al. 1988, 1998a; Contursi et al. 2000).

<sup>1</sup> We also detect a weak and unknown emission feature between 9.3 and 9.9  $\mu\text{m}$ , which seems brighter, relatively to UIBs, in disks than in central regions. However, the very poor signal to noise ratio of disk spectra does not allow us to be conclusive. It cannot be an artefact due to the change of filter since that change occurs after the feature is observed. It is too narrow to be emitted by silicates. The identification with ionized PAHs (*see e.g.* Allamandola et al. 1999) would be inconsistent with the fact that the flux ratio of this feature to classical UIBs seems higher in regions of low radiation density and excitation than in central regions. It is also unlikely that it corresponds to the H<sub>2</sub> rotational line at 9.66  $\mu\text{m}$  since this is characteristic of warm and excited molecular clouds in starburst nuclei (*e.g.* Spoon et al. 2000). Finally, we mention that it also matches in wavelength a feature from the CH<sub>3</sub> functional group at 9.6  $\mu\text{m}$  (Duley & Williams 1981).

While the 7  $\mu\text{m}$  flux in spiral galaxies essentially consists of the UIB emission, the 15  $\mu\text{m}$  filter covers the emission from mainly two dust species: the hot tail of a continuum attributed to very small grains (VSGs) of the order of 0.5–10 nm in size and most often impulsively heated like UIB carriers (Désert et al. 1990), and also UIBs. The red wing of the 11.3  $\mu\text{m}$  band contributes little, but the band at 12.7  $\mu\text{m}$  and the emission plateau that connects it to the 11.3  $\mu\text{m}$  band can be important; the smaller UIB features listed above also contribute, although to a lesser extent. When spatial resolution is high enough, the emission from VSGs and UIB carriers can be clearly separated: around M 17 and in the reflection nebula NGC 7023, the VSG continuum strongly peaks in a layer closer to the excitation sources than the UIBs, inside the ionized region for M 17 (Cesarsky et al. 1996a, 1996b). Therefore, the  $F_{15}/F_7$  flux ratio decreases with increasing distance from the exciting stars of an HII region.

In the spectra of all five galaxies (Fig. 1), the intensity ratios of UIBs are remarkably stable, which is a common property of a variety of astronomical sources (Cohen et al. 1986; Uchida et al. 2000). The only highly varying feature is the VSG continuum that is best seen longward of 13  $\mu\text{m}$ . It has various amplitudes and spectral slopes in galactic nuclei. It remains very modest compared to that in starburst galaxies (Tran 1998; Sturm et al. 2000), and is hardly present in averaged disks. In Paper II, we show that the integrated mid-infrared luminosity of normal spiral disks is dominated by the contribution from photodissociation regions (where the UIB emission is maximum). From a comparison with H $\alpha$  luminosities, we show that this predominance of the photodissociation region emission results in the fact that, when integrated over the disk, the UIB emission is a good tracer of massive young stars.

Finally, as alluded to earlier, a number of fine-structure lines can be present in the mid-infrared spectral range, although their contribution to the broadband flux is always negligible in spirals. In normal galaxies, the most prominent is the [NeII] line at 12.81  $\mu\text{m}$ , which at the spectral resolution of ISOCAM is blended with the UIB at 12.7  $\mu\text{m}$ . No lines from high excitation ions such as [NeIII] at 15.56  $\mu\text{m}$  are convincingly detected, and the [NeII] line at 12.81  $\mu\text{m}$  is weak, since the intensity of the blend with the UIB at 12.7  $\mu\text{m}$ , relative to the isolated UIB at 11.3  $\mu\text{m}$ , is rather stable in different excitation conditions. Some variation however exists. To compare the strength of the [NeII] line in our galaxies to that observed by Förster-Schreiber et al. (2001) in the starburst galaxies M 82, NGC 253 and NGC 1808, we have measured in a similar way the flux of the blend  $F_{12.75}$  above the pseudo-continuum drawn as a straight line between 12.31 and 13.23  $\mu\text{m}$ , and the flux of the 11.3  $\mu\text{m}$  UIB  $F_{11.3}$  with its respective continuum level defined in the same way between 10.84 and 11.79  $\mu\text{m}$ . We find that the energy ratio  $F_{12.75}/F_{11.3}$  of circumnuclear regions decreases from 0.67 in NGC 1365 to 0.60 in NGC 613 and 5236, 0.52 in

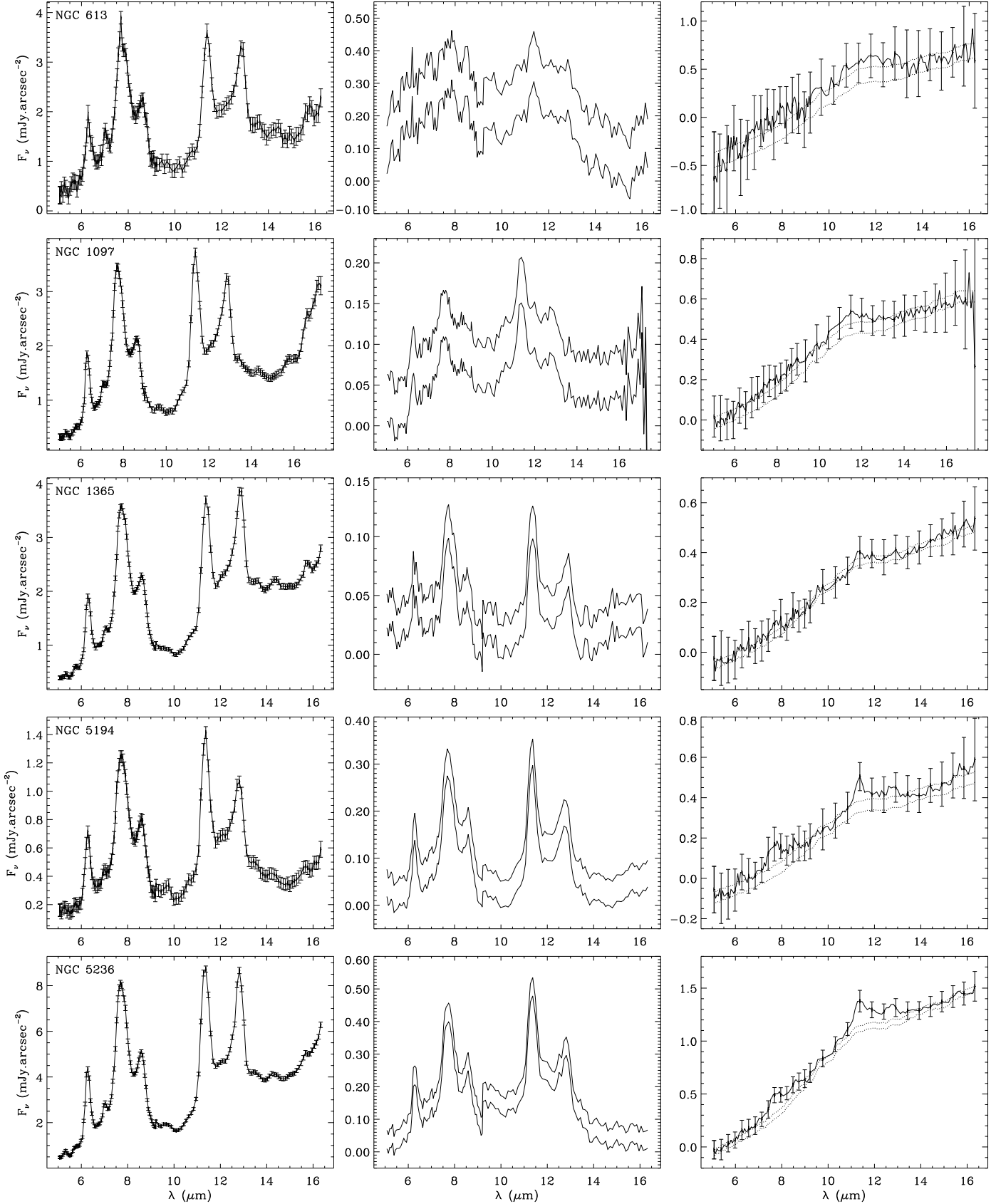


**Fig. 1.** Spectra of central regions (left) and the inner disk (middle). The upper and lower limits are determined from limits on the zodiacal spectrum shown with dotted lines (right), adjusted using the average spectrum of the faintest pixels, also shown with its dispersion. The flux unit for all spectra is  $\text{mJy arcsec}^{-2}$ .

NGC 1097 and 0.47 in NGC 5194; in the averaged inner disks of NGC 1365, 5236 and 5194, where it is still measurable, it takes the approximate values 0.5, 0.45 and 0.4. These figures are much lower than those observed in cores of starburst galaxies by Förster-Schreiber et al. (2001) where it can reach 1.7 and argue for a generally small contribution of [NeII] to the spectra. Adopting as the intrinsic  $F_{12.7}/F_{11.3}$  UIB energy ratio the minimum value of  $F_{12.75}/F_{11.3}$  that we measure in our spectra, *i.e.* 0.4, we obtain a maximum [NeII] equivalent width of  $0.22\text{ }\mu\text{m}$  in the nucleus of NGC 5236. As for the UIBs, their equivalent widths in disks and central regions range respectively between  $\text{EW}(12.7) = 0.3\text{--}0.6\text{ }\mu\text{m}$  and  $\text{EW}(11.3) = 1.2\text{--}1.9\text{ }\mu\text{m}$  (these numbers do not take into account broad UIB wings that occur if the bands are described by Lorentzians). Our estimates give a minimum value for  $F_{12.7}/F_{[\text{NeII}]}$  of 9.2 (in NGC 1365), that we can compare with the results of Sturm et al. (2000) in the starburst galaxies M 82 and NGC 253 from their ISOSWS spectra with a high spectral resolution ( $\lambda/\Delta\lambda \approx 1500$ , versus  $\approx 40$  for ISOCAM). They obtain values of 0.96 and 1.32. The contribution from the [NeII] line to our spectra is thus confirmed to be negligible with respect to starburst galaxies.

## 5. The dependence of $F_{15}/F_7$ on spiral and bar types and comparison with IRAS results

In their infrared analysis, Huang et al. (1996) pointed out that bars are able to significantly enhance the total star formation only in early-type galaxies (mixing all types between S0/a and Sbc). It is also known that bars do not share the same properties all through the Hubble sequence: among early types, or more exactly in spirals with large bulges, since the relationship between Hubble type and bulge to disk ratio is far from direct (*e.g.* Sandage & Bedke 1994; Seigar & James 1998), they tend to be longer (Athanassoula & Martinet 1980; Martin 1995), and their amplitude, with respect to that of the underlying axisymmetric potential, tends to be higher. For instance, Seigar & James (1998), using K band photometry to trace the stellar mass, find that galaxies with the strongest bars have bulge to disk mass ratios between 0.3 and 0.5. For larger bulges, their number of galaxies is too low to derive any meaningful bar strength distribution. Early-type bars host little star formation, except near their ends and at their center, whereas late-type galaxies generally harbor HII regions all along the bar (García-Barreto et al. 1996), which suggests that their shocks are not as strong as in early types (Tubbs 1982). Inner Lindblad resonances between the gas and the density wave, which appear when there is sufficient central mass concentration and when the bar rotates more slowly than  $(\Omega - \kappa/2)_{\text{max}}$  (where  $\Omega$  is the gas circular rotation frequency and  $\kappa$  the epicyclic frequency), and which presence induces straight and offset shocks along the bar (Athanassoula 1992), are also typically expected in early-type galaxies. These structural

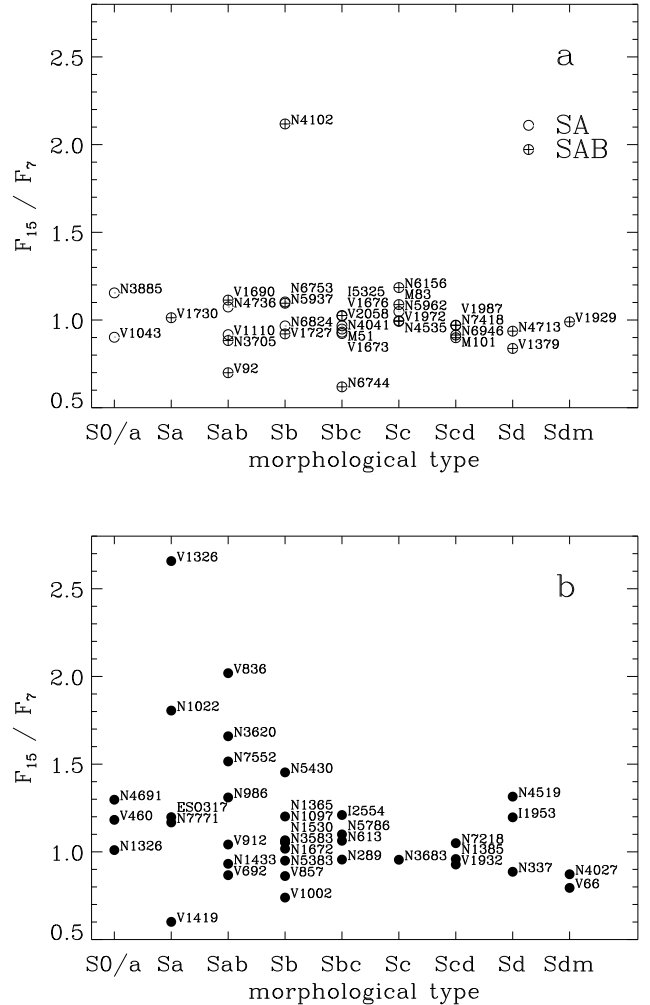


**Fig. 2.** (a): Integrated mid-infrared color  $F_{15}/F_7$  as a function of morphological type for unbarred or weakly barred galaxies, represented respectively by open circles and crossed circles. Virgo galaxies are identified by their VCC number (see Table 1) and others by their NGC number. (b): Same as (a) for strongly barred galaxies.

differences have consequences on the efficiency of bars to drive massive inward gas flows.

We show in Fig. 2a the distribution of  $F_{15}/F_7$  according to morphological type (as given in the RC3) for the control subsample including only SA and SAB galaxies. For this population – excepting NGC 4102<sup>2</sup> –, the mid-

<sup>2</sup> This galaxy shows a peculiar structure, with a central lens-like body or fat oval of moderate length ( $D_{\text{bar}}/D_{25} \approx 0.2$ ) surrounded by an external pseudo-ring probably associated with a Lindblad resonance. NGC 4102 is thus a genuine weakly barred galaxy, and not a SB. However, such a dynamical structure is still efficient to drive inward mass transfer. We also point to the very strong concentration of its mid-infrared emission (see Table 2), a property common to early-type barred spirals (Fig. 6).

infrared color is remarkably constant around a value of 1 (ranging from 0.7 to 1.2). This is rather typical of the color of the surface of molecular clouds exposed to radiation fields ranging from that observed in the solar neighborhood to that found in the vicinity of star-forming regions.  $F_{15}/F_7$  colors observed toward HII regions are typically of the order of 10, while those of photodissociation regions range between 2 and the HII region values (Tran 1998). The fact that  $F_{15}/F_7$  remains of the order of 1 in most galaxies – it also shows generally little variation from pixel to pixel in disks – indicates that, at our angular resolution, emission from HII regions and their immediate surroundings is diluted by the larger neighboring interstellar medium (at a mean distance of 20 Mpc, 3" represent 300 pc). In fact, in the Atlas, we show that even in giant star-forming complexes that can be identified in the maps,  $F_{15}/F_7$  rarely exceeds 2–3.

The case of strongly barred spirals is more complex (Fig. 2b): whereas many of them share the same integrated colors as their unbarred counterparts, an important fraction shows a color excess, the maximum color being above 2.5 instead of 1.2 for SA(B)s. Furthermore, such an excess occurs only among the earliest morphological types, from SB0/a to SBb. Note that in bulges, the envelopes of K-M stars can contribute an important fraction of the mid-infrared emission. However, this would be negligible at  $15\mu\text{m}$  and mostly affect the  $7\mu\text{m}$  band: correcting for such an effect would only re-inforce the observed trend. We also qualify that observation by noting that two galaxies, NGC 1022 and NGC 4691, have likely experienced a merger; gas may therefore have sunk to the center as a result of the violent energy dissipation in the merger, and not simply under the influence of the bar, which actually may have been formed during the interaction. Dismissing these two objects however does not change the fact that the color distribution of the strongly barred galaxies shows  $15\mu\text{m}$  excesses that are absent from that of weakly barred or unbarred spirals.

One can wonder whether cluster galaxies introduce a bias in our sample, because a number of them are perturbed by their environment and thus may have an uncertain morphological type. Koopmann & Kenney (1998) have shown that a significant fraction of early-type spirals in Virgo have been “misclassified” due to their dearth of star formation in the disk. The degree of resolution of spiral arms into star formation complexes is indeed one of the three criteria defining the Hubble sequence, but it is not unambiguously linked to the bulge to disk ratio. Concerning several Virgo members of our sample, the bulge is very small for the attributed type (Sandage & Bedke 1994), in such cases defined mostly by the disk appearance. This is of course related to the anemia phenomenon, due to gas deficiency caused by interaction with the intracluster medium. Of our Virgo galaxies of types S0/a–Sb, 10/14 are HI-deficient, versus 3/9 for types Sbc–Sdm (see Table 1, where  $def > 1.2$  has been adopted as the criterion

for HI deficiency). This apparent segregation with morphological type certainly results from the above classification bias. Thus, differentiating galaxies in Fig. 2 according to their true bulge to disk ratio would cause an under-representation of SA-SAB early-type spirals, which make the crucial part of our comparison sample. If we had to discard completely the early-type SA-SAB subsample, the maximum allowed conclusion from Fig. 2 would be that we observe a color excess in a fraction of early-type strongly barred galaxies, without excluding the possibility of such an excess in early-type non-barred galaxies, in which case another mechanism for mass transfer would have to be thought of.

However, at least five early-type SA-SAB spirals remain which are not HI-deficient and thus unlikely to suffer from the above bias, namely VCC 92 = NGC 4192, NGC 3705, NGC 4736, NGC 5937 and NGC 6824. We do not consider NGC 3885, SA0/a in the RC3, because it looks like a genuine barred galaxy: its bulge is elongated in a direction distinct from the major axis of outer isophotes and crossed by dust lanes; it is furthermore classified as such by Vorontsov-Velyaminov & Arkhipova (1968) and Corwin et al. (1985). These galaxies show no global color excess, like the rest of the SA-SAB subsample, and like a number of bona-fide early-type SB galaxies with normal HI content. Hence, our view should not be too strongly distorted by the classification bias. We have also checked the influence of this bias on HI-deficient barred galaxies with a color excess. On optical images, VCC 836 = NGC 4388 unambiguously resembles classical early-type spirals, with a prominent bulge crossed by thick dust lanes; VCC 460 = NGC 4293 stands between HI-deficient and HI-normal galaxies, and also has an early-type aspect. The case of VCC 1326 = NGC 4491 is not that clear, because it is a low-mass galaxy.

Our sample thus confirms and extends to the ISOCAM bands a phenomenon that was evidenced from IRAS observations by Hawarden et al. (1986) and Huang et al. (1996), namely that a significant fraction of SB galaxies can show an excess of  $25\mu\text{m}$  emission (normalized to the emission at 12 or  $100\mu\text{m}$ ) compared with SA and SAB galaxies. The case of SAB galaxies is in fact unclear: some of them show such an excess according to Hawarden et al. (1986), but they are indistinguishable from SAs in the analysis of Huang et al. (1996). From the present ISO-CAM data, it already appears that indeed SA and SAB galaxies share similar mid-infrared properties.

In order to compare more directly our results with IRAS-based results, Fig. 3 shows the relationship between  $F_{15}/F_7$  and  $F_{25}/F_{12}$ . For  $\log(F_{25}/F_{12}) < 0.3$  (which is close to the value given by Hawarden et al. (1986) as the limit for the presence of a  $25\mu\text{m}$  excess),  $F_{15}/F_7$  shows no systematic variation and SA, SAB and SB galaxies are well mixed. Above that threshold, SB galaxies strongly dominate (the SAB galaxy with high colors is NGC 4102) and the  $F_{15}/F_7$  ratio follows the increase of  $F_{25}/F_{12}$ . Given the

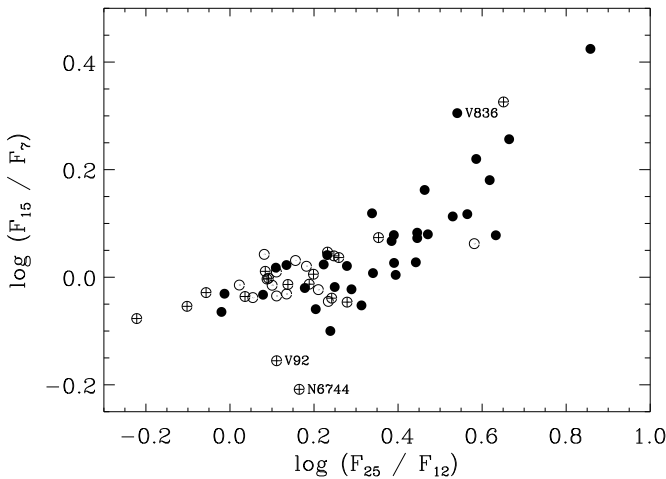


**Fig. 3.** Comparison of mid-infrared colors from ISO ( $F_{15}/F_7$ ) and IRAS ( $F_{25}/F_{12}$ ).  $F_{25}$  always contains the VSG emission (see Sect. 4) whereas at low temperatures,  $F_{15}$  is dominated by UIBs, which explains the constancy of  $F_{15}/F_7$  below a threshold of  $F_{25}/F_{12} \simeq 2$ . The same convention as in Fig. 2 applies for the representation of SA, SAB and SB classes. We have indicated the names of the Sy2 galaxy NGC 4388 = VCC 836 (see Sect. 7.1), and of the two galaxies with the lowest  $F_{15}/F_7$  colors (note that NGC 6744 was not entirely mapped and that its integrated color is likely a lower limit).

nature of dust components whose emission is covered by the  $7\mu\text{m}$  to  $25\mu\text{m}$  filters (Sect. 4), this behavior can be explained as follows. The classical interpretation for the variation of  $F_{25}/F_{12}$  is that it increases with the radiation field due to the stronger contribution of VSGs to the  $25\mu\text{m}$  than to the  $12\mu\text{m}$  emission, which collects mostly UIB emission (Désert et al. 1990; Helou 1986). The fact that the  $F_{15}/F_7$  ratio remains insensitive to the variation of  $F_{25}/F_{12}$  for  $\log(F_{25}/F_{12}) < 0.3$  implies that in this regime, VSGs provide little flux to both ISOCAM bands as well. Past this threshold, the increase of  $F_{15}/F_7$  signals that the VSG continuum has entered the  $15\mu\text{m}$  bandpass and contributes an ever increasing fraction.

The galaxies with a  $15\mu\text{m}$  excess ( $F_{15}/F_7$  above 1.2, or 0.08 dex) also distinguish themselves from the rest of our sample by having on average larger far-infrared to blue luminosity ratios. For this subsample,  $L_{\text{FIR}}/L_B$  spans the range [0.6; 7.3] with a logarithmic mean of 2.2 and dispersion by a factor 2.2, while  $L_{\text{FIR}}/L_B$  of the complementary subsample falls in the interval [0.2; 9.0], has a logarithmic mean of 0.9 and dispersion by a factor 2.4. However, the  $15\mu\text{m}$ -excess galaxies have far-infrared luminosities that are equivalent to those observed in the rest of the sample. Hence, in these galaxies with a VSG emission excess, a higher fraction of the total emission is reprocessed in the whole infrared range. There is also a slight difference, al-

though not statistically significant, between SBs with no  $15\mu\text{m}$  excess and SA-SAB galaxies: the  $L_{\text{FIR}}/L_B$  logarithmic means and dispersion factors are 1.1 and 2.7 for SBs with no excess, and 0.8 and 2.2 for SAs-SABs.

That mid-infrared color excesses occur only in SB galaxies indicates that somehow, a global increase of the interstellar radiation field intensity is linked to the presence of a strong bar, although this condition is clearly not sufficient. The fact that many barred galaxies earlier than SBb appear very similar in their integrated color to their unbarred counterparts means that no simple link exists between the bar class, the bulge-to-disk ratio and the onset of a starburst in normal spirals. Several intervening parameters can be thought of: the true strength of the bar in dynamical terms (the separation into SB and SAB classes is subjective and too rough, and in a recent study, Buta & Block 2000 show that the SB class includes a wide range of actual bar strengths); the available gas content inside corotation; the star formation efficiency along bars and in central regions; the timescales for starburst activation and exhaustion; interaction with a companion or with the intracluster gas. Some of these effects can be investigated in the present sample. We will discuss them in Sect. 7, but first we turn our attention to mid-infrared properties of the central regions, as defined in Sect. 3 and in the Atlas.

## 6. The role of central regions

As the presence of a bar is expected to influence the star formation in the circumnuclear region and much less in the disk (except in the zone swept by the bar), we are naturally led to emphasize the relative properties of nuclei and disks. Maps shown in the Atlas demonstrate that central regions, observed in the infrared, are prominent and clearly distinct from other structures, much more than on optical images.

In Fig. 4 we plot the fraction of the total  $15\mu\text{m}$  flux originating from the central region (inside the radius  $R_{\text{CNR}}$ ) as a function of the global  $F_{15}/F_7$  color. Galaxies for which a central region could not be defined on the mid-infrared brightness profiles are also shown, and are attributed a null central fraction. Galaxies are not distributed at random in this plot, but rather on a two-arm sequence that can be described in the following way: (1) high  $F_{15}/F_7$  colors are found exclusively in systems where a high fraction of the flux is produced in the circumnuclear regions; (2) galaxies with small  $F_{15}/F_7$  ratios ( $< 1.2$ ) are found with all kinds of nuclear contributions.

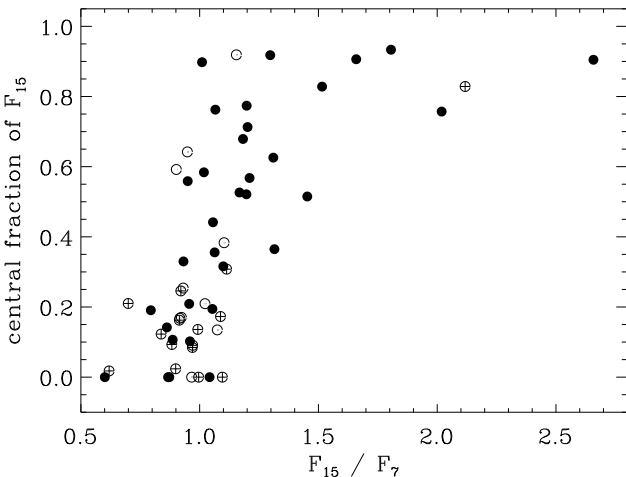
The bar class appears to play a part in the location of galaxies in this diagram, although this is not clear-cut: all galaxies with high circumnuclear contribution ( $> 40\%$ ) and large  $F_{15}/F_7$  colors ( $> 1.2$ ) are SB galaxies, apart from NGC 4102, while SA-SAB galaxies are quite indistinguishable from one another and cluster in the small nuclear contribution ( $< 30\%$ ) and low  $F_{15}/F_7$  color cor-

ner of the graph. There is also a clear preponderance of SB galaxies in all the centrally dominated range. Only two SA-SAB galaxies show very high concentration fractions, NGC 3885 and NGC 4102. The latter galaxy was already discussed; for NGC 3885, strong indications exist that its bar class is incorrect (see the discussion in Sect. 5).

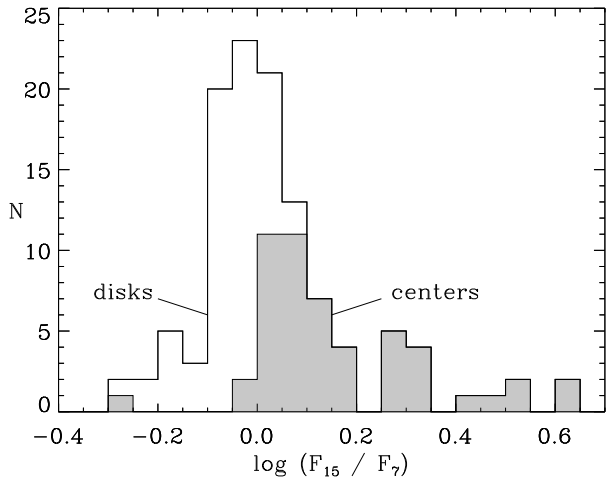
However, it is quite significant that SB galaxies cover both sequences in Fig. 4 and in particular are found all through the sequence of varying flux concentration and low  $F_{15}/F_7$  color. Therefore, Fig. 4 shows that high global  $F_{15}/F_7$  colors require that the flux concentration be high, and that the galaxy be SB, but none of these two properties is enough to predict that the global  $F_{15}/F_7$  ratio will be high. To understand the importance of the flux concentration, let us first study separately the colors of central regions and those of disks.

Fig. 5 compares the  $F_{15}/F_7$  distributions observed in the disk and in the central regions of our galaxies (whenever the radius of the central regions  $R_{\text{CNR}}$ , fitted on  $7\mu\text{m}$  brightness profiles, could not be defined, the galaxy has been considered as a pure disk). These histograms indicate that  $F_{15}/F_7$  ratios of circumnuclear regions are higher than those of disks (and this is a systematic property, verified for each individual galaxy except NGC 4736 and 6744, whose central regions are dominated by old stellar populations). Colors of disks are fairly constant and close to the integrated colors of SA-SAB galaxies ( $F_{15}/F_7 = 0.89 \pm 0.14$  for the  $1\sigma$  dispersion), whereas circumnuclear colors form a broader distribution extending towards high values ( $F_{15}/F_7 = 1.59 \pm 0.78$ ).

The cause for this difference of colors can easily be seen in the spectra of Fig. 1: in all spectra with sufficient signal-



**Fig. 4.** Relationship between the central flux fraction at  $15\mu\text{m}$  and the integrated  $F_{15}/F_7$  color. Galaxies with no identifiable central regions, *i.e.* surface brightness profiles consistent with a single disk component, have been placed at a null ordinate.



**Fig. 5.** Compared histograms of  $F_{15}/F_7$  colors averaged in disks and in circumnuclear regions. The galaxies used are respectively those whose disk is not strongly contaminated by the central component (the excluded galaxies are NGC 1022, NGC 4691, VCC 1419 = NGC 4506, NGC 1326 and NGC 3885), and those with central regions that could be adjusted on surface brightness profiles (otherwise the galaxy is considered to be composed only of a disk). The isolated galaxy with a very low central color is NGC 6744, which is clearly devoid of young stars all inside its inner ring.

to-noise ratio, the relative intensities of the UIBs are almost unchanged from galaxy to galaxy, or from central regions to disks. On the contrary, the level and spectral slope of the continuum seen longward of  $13\mu\text{m}$  is highly variable and always stronger in the central regions than in the disks. This continuum is attributed to VSGs (see Sect. 3) and its presence in the  $15\mu\text{m}$  band is a characteristic sign of intense star formation (*e.g.* Laurent et al. 2000).

The reason why high global  $F_{15}/F_7$  colors require a high flux concentration can be directly derived from Fig. 5: only the central regions of galaxies are able to reach high  $F_{15}/F_7$  colors, and they have to dominate the integrated emission to affect the global color. Furthermore, the fact that the two color histograms overlap explains why a high flux concentration does not necessarily imply a high  $F_{15}/F_7$  color.

We however still have to identify the property or properties required, in addition to belonging to the SB class, for a galaxy to show a high mid-infrared flux concentration. We have seen in Fig. 2 that the morphological type plays a major part in the presence of high colors. Fig. 6 shows the evolution of the concentration fraction as a function of morphological type. It confirms that for SB galaxies, there is a definite trend for the central flux fraction to rise as the morphological type gets earlier. More precisely, SB

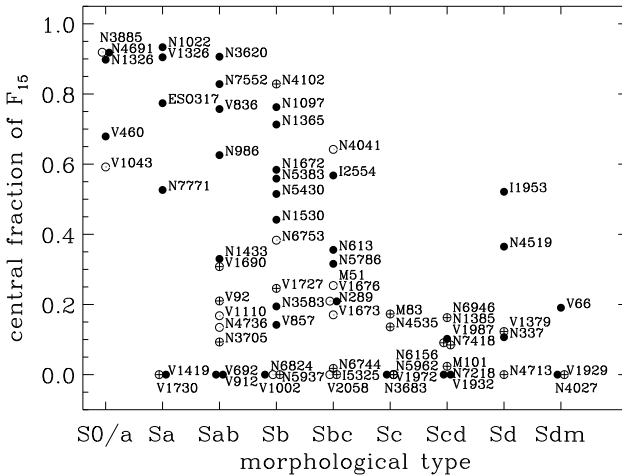


**Fig. 6.** Fraction of total  $15\mu\text{m}$  fluxes arising from the central condensation, as a function of morphological type. As in Fig. 4, galaxies with no identifiable central regions have been placed at a null ordinate. The central fraction of  $F_7$  fluxes, not shown here, has a very similar behavior, with only slightly lower values.

galaxies with central fractions greater than 40% are found predominantly among galaxies earlier than Sb.

It is less clear in Fig. 6 whether SA-SAB galaxies follow a similar or a different trend, partly because of the lack of such bar classes in our sample for types S0/a and Sa, and also because types Sab and Sb may be incorrect due to the morphological classification bias affecting cluster galaxies, as already discussed in Sect. 5. In that section however, we emphasized the existence of a set of five early-type SA-SAB spirals which do not suffer from morphological misclassification: VCC 92 = NGC 4192, NGC 3705, NGC 4736, NGC 5937 and NGC 6824. As apparent in Fig. 6, they all have a low central flux fraction, much lower than that observed in SB galaxies in the same range of types. This supports the view that the trend seen for increasing concentration fraction with earlier type concerns only SB galaxies (or peculiar objects like VCC 1043), SA-SAB galaxies having a generally low concentration factor whatever their type.

We can summarize our findings in this section in the following way: integrated  $F_{15}/F_7$  colors of galaxies are generally of the order of 1. However,  $F_{15}/F_7$  is often higher in central regions. Spiral galaxies with high  $F_{15}/F_7$  colors must simultaneously be (1) dominated by their central regions, (2) of bar type SB, and (3) of morphological type earlier than Sb. However, the reverse is not true: as can be seen in Fig. 6, NGC 5383 (a Markarian galaxy), 1672, 1365 and 1097 for instance fulfill these conditions – between 55 and 75% of their  $15\mu\text{m}$  radiation comes from small central regions (respectively 17, 8, 6 and 8% of the optical diameter) – yet their  $F_{15}/F_7$  color is very similar to that of

disk-dominated galaxies. This suggests that they host at their center larger concentrations of gas and dust than in the average of galaxies of the same Hubble type, but for some yet undetermined reasons, they presently undergo smooth star formation instead of a nuclear starburst. We propose that either the net gas inflow rate to the center has decreased (due to a slower replenishment from the inner disk which would have been previously partially depleted in gas, or a smaller efficiency of the evolved bar to make gas lose its angular momentum) or, since star formation bursts occur on a much shorter timescale than bar life, that we are imaging these objects at a period of quiescence in-between bursts. Concerning this last point, see the results of the simulations of Martinet & Friedli (1997) and the population synthesis estimates of Kotilainen et al. (2000) for the circumnuclear rings of NGC 1097 and 6574.

## 7. Origin of the circumnuclear infrared excess

### 7.1. Non-stellar activity

Of the SB galaxies, four are known to host a Seyfert nucleus: in order of decreasing flux fraction from the central condensation, VCC 836 = NGC 4388, NGC 1365, NGC 1097 and NGC 1433. For these, the high central color could arise from dust heated by non-stellar radiation from the accretion disk and halo of the central object and would thus not necessarily indicate the presence of massive stars. For NGC 1097, we have the direct visual evidence that the contribution from the active nucleus to the circumnuclear emission is negligible, since the central mid-infrared source is resolved into the well-known star-forming ring, which is very bright, and a faint point source at the nucleus. Correcting the images of NGC 1097 for dilution effects with a procedure analog to CLEAN (see the Atlas for more detail), we obtain fractions of the total circumnuclear fluxes contributed by the nuclear point source of less than 3% at  $7\mu\text{m}$  and about 1% at  $15\mu\text{m}$ . This central source was measured inside a radius of  $3''$ , while the ring extends between radii  $\approx 6''$  and  $12''$ .

We can also inspect the low-resolution spectra between 5 and  $16\mu\text{m}$  of the central regions of NGC 1097 and 1365 (left column of Fig. 1). Indeed, Genzel et al. (1998) and Laurent et al. (2000) have shown that a strong continuum at  $5\mu\text{m}$  and small equivalent widths of the UIBs are signatures of dust heated by an active nucleus. Yet all our spectra are similar to that of the inner plateau of NGC 5194 ( $\approx 50''$  in diameter) – which also contains a weak Seyfert nucleus, but completely negligible – and to that of NGC 5236: they are dominated by UIBs in the  $5\text{--}10\mu\text{m}$  range and the underlying continuum at  $5\mu\text{m}$  is comparatively very low. We conclude that in these galaxies, the contribution of non-stellar heating to the emission observed inside  $R_{\text{CNR}}$  is small.

The cases of NGC 4388 and NGC 1433 can only be discussed on the basis of imaging results. The central condensation of NGC 1433 is large (we have determined a

diameter of  $31'' \approx 1.7$  kpc) and extremely smooth, much flatter than the point spread function: we therefore consider unlikely a major contribution from the LINER/Seyfert nucleus, which should manifest itself as a point source. For NGC 4388, we cannot conclude and the active nucleus may be dominant. We can only mention that its global color is lower than that of VCC 1326 = NGC 4491, and this is marginally true as well for the nucleus, and that the nucleus of VCC 1326 is not classified as active<sup>3</sup>.

Hence, the presence of Seyfert nuclei does not modify our interpretation that high mid-infrared colors in the present sample are not due to dust heated by non-stellar photons and should rather signal the existence of central starbursts.

## 7.2. Circumnuclear starbursts

We now examine the most likely cause of the  $15\mu\text{m}$  emission excesses detected in our sample, central starbursts triggered by the bar dynamical effects. We warn that NGC 1022 and NGC 4691 should be considered apart: their dust emission comes almost exclusively from central regions of  $\approx 1$  kpc, but this is more likely due to a past merger than to the influence of the bar, which may have been formed or transformed simultaneously as the starburst event was triggered.

### 7.2.1. Available molecular gas

To see if a significant difference exists between the central molecular gas content of circumnuclear starburst galaxies and quiescent ones, we have searched the literature for single-dish CO(1-0) data in the smallest possible beams. Single-dish data are better suited to our purpose than interferometric data since the latter are scarcer and do not collect all the emission from extended structures. The conversion of CO antenna temperatures to molecular gas masses is approximate for two main reasons: the  $\text{H}_2$  mass to CO luminosity ratio varies with metallicity and physical conditions; and the derivation of CO fluxes requires the knowledge of the source structure, because it is coupled to the antenna beam to produce the observed quantity which is the antenna temperature.

Sensible constraints on the structure of CO emission can be drawn from that observed in the mid-infrared. As dust is physically associated with gas, the mid-infrared emission spatial distribution should follow closely that of the gas, but be modified by the distribution of the

<sup>3</sup> Far-infrared diagnostics of nuclear activity are ambiguous for NGC 4388: its infrared to radio flux ratio as defined by Condon et al. (1991) is  $q = 2.27$ , and its spectral index between 25 and  $60\mu\text{m}$  (de Grijp et al. 1987) is  $\alpha = 1.23$ . Both values indicate that stellar and non-stellar excitations may contribute in comparable amounts to the infrared energy output. Concerning VCC 1326, its spectral index between 25 and  $60\mu\text{m}$ ,  $\alpha = 1.67$ , is rather typical of starbursts.

star-forming regions that provide the heating, and which are likely more concentrated than the gas reservoir. Since gaussian profiles provide an acceptable description of most infrared central regions at our angular resolution, we have therefore assumed that the CO emitting regions are of gaussian shape, with half-power beam width (HPBW) between one and two times that at  $7\mu\text{m}$ . The  $7\mu\text{m}$  HPBW were derived by matching gaussian profiles convolved with the point spread function to the observed  $7\mu\text{m}$  profiles<sup>4</sup>.

To find the meaning of various antenna temperatures (with various corrections) and which conventions are used in the literature, the explanations of Kutner & Ulich (1981) and Downes (1989) were of much help. We converted given temperatures to the  $T_R^*$  scale<sup>5</sup>. We then attempted a correction of antenna to source coupling, assuming a gaussian source and a gaussian diffraction pattern with angular standard deviations  $\theta_S$  and  $\theta_B$ . The relationship below follows for the source brightness temperature  $T_b$ , which is averaged over the beam in the observation, whereas we want to recover its intrinsic value over the source extent:

$$T_R^* \times (\theta_S^2 + \theta_B^2) = T_b \times \theta_S^2.$$

Table 1 contains the beam width of the observations and the derived  $\text{H}_2$  masses for the adopted references. A conversion factor  $f = N(\text{H}_2) / I(\text{CO}) = 2.3 \cdot 10^{24} \text{ molecules m}^{-2} (\text{K km s}^{-1})^{-1}$  (Strong et al. 1988) has been used to compute the mass as:

$$M_{\text{H}_2} / (2m_H) = f \times \int T_b dV (\text{K km s}^{-1}) \times 2\pi (\theta_S D)^2 \times (1 - \exp(-\frac{1}{2}(\alpha_{\text{CNR}} / \theta_S)^2))$$

where  $m_H$  is the hydrogen atom mass and  $D$  the distance (in m). In the above formula, we estimate the mass only inside the angular radius  $\alpha_{\text{CNR}}$  used for the infrared photometry of circumnuclear regions. Only when the central regions are resolved and mapped is there no need to assume a brightness distribution.  $\text{H}_2$  masses derived in this way are probably not more precise than by a factor three, including the dispersion of the factor  $f$ , but the dynamic range in the sample is still sufficient to allow a discussion of the results.

<sup>4</sup> In NGC 1530, the scales of the molecular gas and infrared concentrations are of the same order. In NGC 1022, the source HPBW is estimated to be  $\approx 17''$ , which is  $\approx 2.9$  times that of the innermost infrared regions. However, these are clearly more extended than a central gaussian and not representative of normal CNRs, since likely gathered by a merger. For this and other galaxies whose central regions are clearly structured (*i.e.* NGC 1097 and NGC 4691), detailed CO maps where the source is resolved were used. It is also the case for NGC 1530, 5236 and 6946.

<sup>5</sup> which includes corrections for atmospheric attenuation and all instrumental effects except antenna to source coupling.

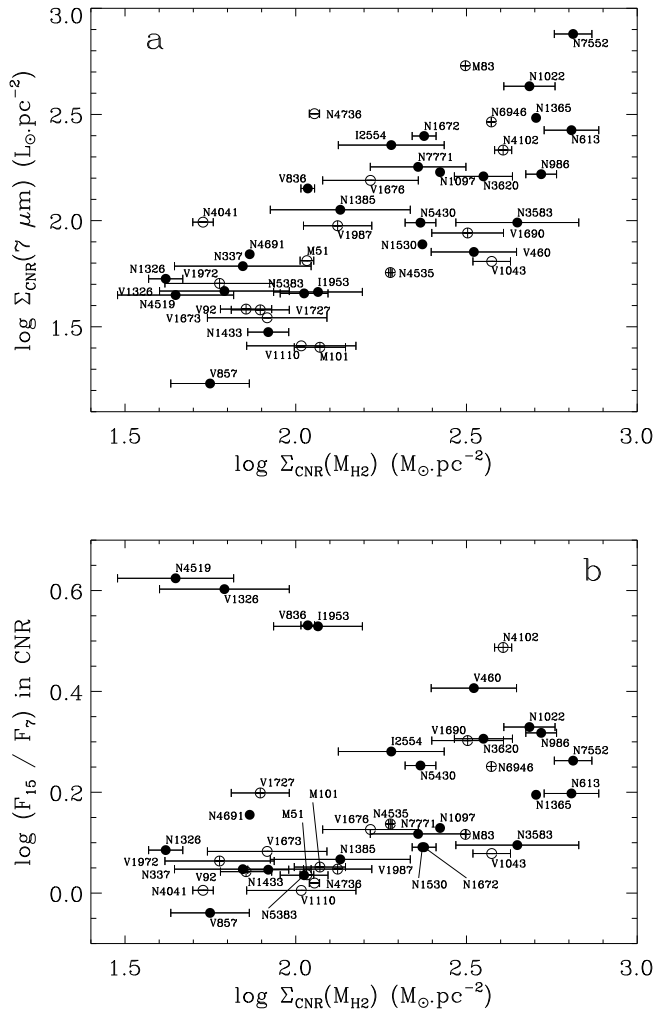


**Fig. 7.** (a):  $7\mu\text{m}$  surface brightness as a function of the average  $\text{H}_2$  surface density, both inside the circumnuclear regions defined by mid-infrared photometry (CNR). The limits on  $\text{H}_2$  mass are not true error bars, but simply indicate the effect of varying the scale of the gaussian distribution from once to twice that measured at  $7\mu\text{m}$  (see text). (b):  $F_{15}/F_7$  color as a function of the average  $\text{H}_2$  surface density, both inside the CNR, with the same convention for error bars as in (a).

Although the beam of CO observations is in general larger than  $\alpha_{\text{CNR}}$ , it remains (except for NGC 337) smaller than the diameter of the bar which collects gas from inside corotation, believed to be located close to the end of the bar (Athanassoula 1992), so that it is still meaningful to compare our measurements on infrared condensations to CO data.

Fig. 7a shows the variation of the  $7\mu\text{m}$  surface brightness as a function of the average molecular gas surface density inside  $R_{\text{CNR}}$ . Higher densities of the molecular material are associated with an increase in the infrared

brightness of the central regions. This is expected, since the amount of dust scales with that of gas, which essentially consists of the molecular phase in central regions of galaxies. More interesting is Fig. 7b where we show the evolution of the  $F_{15}/F_7$  color inside  $R_{\text{CNR}}$  as a function of the same quantity as in Fig. 7a. For the majority of our sample,  $F_{15}/F_7$  tends to rise, within a very large dispersion, when the molecular gas mean density increases (it roughly doubles when the  $\text{H}_2$  surface brightness varies by 1.2 dex). However, a few galaxies dramatically depart from this trend: for colors higher than 2.5 ( $\log F_{15}/F_7 > 0.4$ ), there is a reversal in the sense that hot circumnuclear regions seem to be depleted in molecular gas, with respect to the normal  $\text{H}_2$  content–color distribution.

Although one can think of several reasons why their molecular content may be underestimated (the standard conversion factor may not apply for these galaxies due to their starburst nature or possibly due to a lower metallicity), it is unlikely that this is the case. First, the implied underestimation factors appear quite large, at least 4 to 10. Second, if we were to correct the  $\text{H}_2$  masses by these factors to bring the galaxies within the trend observed in Fig. 7b, then these objects would become abnormal in Fig. 7a, with a deficit of  $7\mu\text{m}$  emission<sup>6</sup>. The four deviating galaxies do not share a common property which would make them special with respect to all the others. NGC 4519 and IC 1953 are similar SBd galaxies, VCC 1326 = NGC 4491 is a small and low-luminosity SBa, and VCC 836 = NGC 4388 is an edge-on Seyfert SBab (for which the molecular content may be ill-determined due to the integration of the CO line throughout the disk).

We thus propose the following interpretation for the galaxies that wander off the main trend in Fig. 7b: the main distribution corresponds to galaxies where the central starburst is more and more intense, as indicated by the high gas surface densities and colors. Galaxies at the turnover of the sequence may be observed in a phase of their starburst (not necessarily common to all galaxies) when it has consumed or dispersed most of the accumulated gas, because of a higher star formation efficiency. This suggests an interesting analogy with HII regions, for which the distinction between “ionization-bounded” and “density-bounded” is made (see Whitworth 1979, also for a discussion of the efficiency of molecular cloud dispersal by young stars). Dust should then be depleted too; however, because of the presence of massive stars, the remaining dust is exposed to a very intense radiation field and reaches a high  $F_{15}/F_7$  color. This ratio may also increase due to the fact that the dust which was mixed with rather dense molecular clouds, of low  $F_{15}/F_7$  color, has been dispersed too. Alternatively, the concentrations of molecular gas in these galaxies may be more compact than in the others and diluted in our large beam (we cannot exclude

<sup>6</sup> Note that it is however conceivable that a fraction of UIB carriers are destroyed, which would cause such a deficit.

that the mid-infrared distribution includes an unresolved core which dominates the color). A confirmation of the above scenario clearly requires better measurements of the central gas content and high-resolution characterization of the starbursts.

Leaving the four galaxies in the upper left quadrant of Fig. 7b apart, the data support an interpretation in terms of starburst with standard properties: the infrared activity in galactic centers can be stronger when the available molecular gas is denser.

### 7.2.2. Color of the central concentration and age of the starburst

Fig. 8 indicates how the  $F_{15}/F_7$  color inside  $R_{\text{CNR}}$  varies with the  $15\text{ }\mu\text{m}$  surface brightness in the same aperture. In principle, the mid-infrared surface brightness can increase either because the amount of dust in the considered area is higher (such as observed in Fig. 7a), or because the energy density available to heat the dust increases. The trend for higher  $F_{15}/F_7$  ratios at large  $15\text{ }\mu\text{m}$  surface brightnesses seen in Fig. 8 indicates that indeed, the increase of the  $15\text{ }\mu\text{m}$  surface brightness is at least partly due to rise of the mean energy density in the CNR. In this diagram again, the galaxies with a peculiar behavior in Fig. 7b stand apart, well above the locus defined by the least absolute deviation fit<sup>7</sup> (dashed line). This supports the fact that the trend seen in Fig. 7b is not due to an underestimation of the  $\text{H}_2$  content, and lends further credit to the interpretation presented in Sect. 7.2.1.

Another study by Dale et al. (1999) has already dealt with the joint variations of mid-infrared surface brightnesses and colors. However, contrary to Fig. 8 where the surface brightnesses and colors are those of the same physical region (the CNR) in a large sample of galaxies, in the Dale et al. (1999) study, resolution elements inside the target galaxies are first binned according to their surface brightness before the mean color of the bin is computed. As a result, a bin does not correspond to a physical object. We simply note that if galactic central regions are binned by surface brightness in Fig. 8, then the obtained mean locus is comparable to those shown by Dale et al. (1999).

The galaxies with the highest central  $F_{15}/F_7$  colors ( $F_{15}/F_7 > 2.5$ ) and which stray from the main trend are barred, but their bars are of moderate lengths (once deprojected and normalized by the optical diameter). In NGC 4519, NGC 4102, VCC 1326 = NGC 4491 and IC 1953, for which it could be estimated,  $D_{\text{bar}}/D_{25} \approx 0.2-0.3$ , when this ratio ranges between 0.06 and 0.67 in galaxies with measurable bar length. This confirms that the central activity, signalled by a high  $F_{15}/F_7$  color, is not

<sup>7</sup> We give this name to a fit where the quantity to be minimized is the sum of absolute values of the distances between the data points and the line. This method is less sensitive to outliers than the least squares fit.

an increasing function of bar strength, as can be expected from the different timescales for star formation and bar evolution.

Since the bar strength alone is not sufficient to explain the observed mid-infrared colors, and since the observational uncertainties are much smaller than the scatter present in Fig. 8, one may suspect that part of this scatter is due to intrinsic properties of each of the circumnuclear starbursts considered. Indeed, given that mid-infrared emission likely traces star formation on timescales longer than, for instance, recombination lines, it is reasonable to expect that for similar mid-infrared brightnesses (corresponding to similar gas and energy densities), the mid-infrared color could vary as a function of the age of the stellar populations responsible for dust excitation. Since star formation does not happen instantaneously all through a  $\approx 1\text{ kpc}$  region and likely occurs in cycles triggered by instabilities, these stellar populations are multiple and their ages should be weighted to reflect the successive generations of stars contributing to dust heating.

Using the population synthesis results of Bonatto et al. (1998), based on ultraviolet spectra between 1200 and  $3200\text{ }\text{\AA}$ , we can estimate the mean stellar age in the central  $10'' \times 20''$ , weighted by the fraction of luminosity emitted at  $2650\text{ }\text{\AA}$  by different population bins. This was possible for eleven galaxies of our sample in common with the

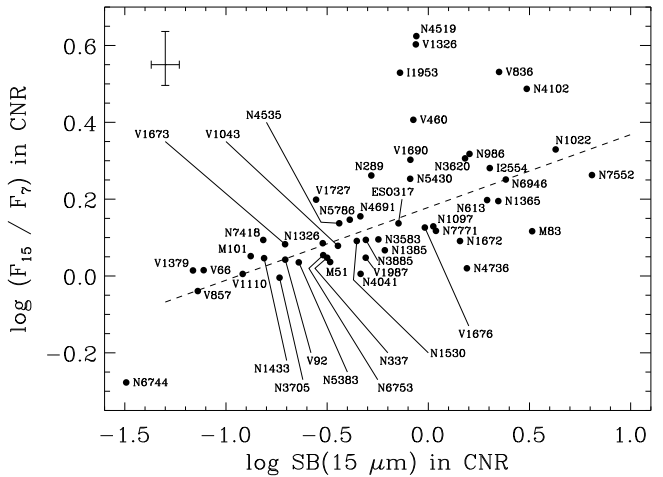


**Fig. 8.** Variation of the mid-infrared color with the  $15\text{ }\mu\text{m}$  surface brightness (in  $\text{mJy arcsec}^{-2}$ ), both inside the same aperture centered on circumnuclear regions. The mean error bar is shown in the upper left corner. The average location of disks in the diagram in terms of average color and global surface brightness (the disk area being delimited by the blue isophote  $\mu_B = 25\text{ mag arcsec}^{-2}$ ) would be at  $(-2.2, -0.05)$ . The dashed line represents the formal least absolute deviation fit, performed including all the galactic central regions (used to define the “color deviation” in Fig. 9).

sample of Bonatto et al. (1998). We compare in Fig. 9 this mean age to the  $F_{15}/F_7$  color deviation, defined as the difference between the observed color and that predicted by the mean distribution of all galaxies (indicated by the least absolute deviation fit in Fig. 8) at the same  $15\mu\text{m}$  surface brightness. For this purpose, we performed the mid-infrared photometry in a slit aperture identical to that used by Bonatto et al. (1998). We indeed see that the younger the weighted age, the higher the central  $F_{15}/F_7$  color deviation. This is thus in agreement with our hypothesis that much of the color variations in Fig. 8 may be due to age variations of the exciting populations.

There are grounds to think that some scatter in Fig. 9 is due to the methodology adopted by Bonatto et al. (1998) in their study. They have grouped galaxies of their sample according to spectral resemblance, morphological type and luminosity, and co-added all UV spectra of each group in order to increase the signal to noise ratio before performing the population synthesis. However, it may not be fully justified to average spectra of different galaxies with the same overall shape but different spectral signatures. A further drawback of this study is that it cannot properly take into account extinction, because of the limitation to a small spectral range in the UV: the derived very low extinctions are meaningless. That is why the two galaxies departing from the well-defined trend described above could owe their age to the method rather than to their intrinsic properties:

- VCC 1690 = NGC 4569 is assigned the same large weighted age as NGC 7552 (their UV spectra are co-added), but has a higher color excess with respect to the mean distribution in Fig. 8. In fact, Maoz et al. (1998) detected very strong P Cygni absorption lines of high-excitation ions (CIV, SiIV, Nv) characteristic of the winds of massive young stars ( $< 6$  Myr), and its spectrum between 1220 and 1590 Å is nearly identical to that of the starburst NGC 1741B.
- NGC 1433 is co-added with NGC 4102, which results in a small weighted age. Yet its color excess is much lower than that of NGC 4102 and more comparable to that of NGC 7552. There is some evidence that the extinction in the central regions of NGC 1433 is much lower than in other galaxies: whereas available Balmer decrement measures indicate  $\text{H}\alpha$  absorptions of the order of 2–3 in other nuclei, the decrement given by Diaz et al. (1985) for NGC 1433 indicates  $A(\text{H}\alpha) \approx 0.9$ . Even if the Balmer decrement is not a good extinction measure, it is instructive to compare values in different galaxies. We also notice that NGC 1433 is the only one among strongly barred spirals which has an amorphous circumnuclear region, with no hot spot that would indicate the presence of massive stellar clusters.

To conclude, Fig. 8 is a strong indication that the mid-infrared emission in circumnuclear regions is influenced by successive episodes of star formation over relatively long

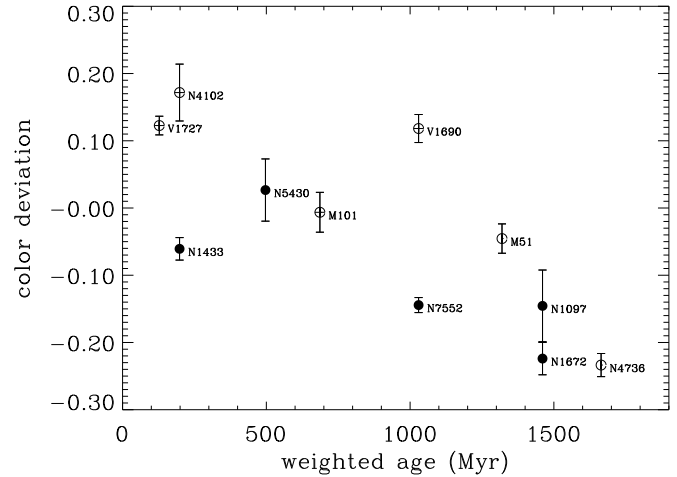


**Fig. 9.** The abscissa indicates the mean age of stellar populations, according to the synthesis results of Bonatto et al. (1998), including the first six elements of their base, stellar clusters to which they attribute ages between 0 and 0.7 Gyr for the first five and in the interval 0.7–7 Gyr for the last one, but excluding the oldest element, an elliptical bulge representing ages between 7 and 17 Gyr. The ages are weighted by the fraction of the flux at 2650 Å that each different population emits. The contribution from continuous star formation has been approximated by a constant flux fraction (equal to the minimum value) and subtracted, in order to consider only successions of bursts. The ordinate is the difference between the measured  $F_{15}/F_7$  color and the color expected from the mean relationship between central surface brightnesses and colors shown in Fig. 8. For this graph, the photometry was performed inside the same apertures as in Bonatto et al. (1998),  $10'' \times 20''$ , and error bars show the effect of varying the slit orientation, which is not given by Bonatto et al. (1998).

periods of time: on the mean, the  $F_{15}/F_7$  color is a sensitive function of the mid-infrared surface brightness, but this relationship is modulated by the mean age of the stellar populations. A striking example of this is NGC 4736. Its central mid-infrared brightness is in the high range, but its central  $F_{15}/F_7$  ratio is low, in accordance with its large mean stellar age confirmed by Taniguchi et al. (1996). From optical population synthesis, they find that a central starburst occurred about 1 Gyr ago in this galaxy, and that subsequent nuclear star formation has proceeded at a low rate.

Combining this result with that of Sect. 7.2.1, we can form the following sketch of what determines the mid-infrared properties of circumnuclear regions: the central surface brightness is connected to the amount of gas, as expected if gas-to-dust ratios are relatively constant. However, accumulation of gas in the center allows the trigger-

ing of intense star formation, so that the interstellar radiation field increases, reflected in higher  $F_{15}/F_7$  ratios. Fig. 8 and 9 suggest then that deviations from this simple description can be related to the star formation history of the circumnuclear regions. On-going starbursts produce excess  $F_{15}/F_7$  colors, while faded starbursts are associated with  $F_{15}/F_7$  deficits.

Additional variation in mid-infrared colors may arise from differences in metallicity and in the compactness of the starburst, with consequences on the amount and nature of the dust, but this is out of the scope of the present study.

## 8. Summary and conclusions

We have studied the mid-infrared activity induced by bars in a sample of 69 nearby spiral galaxies with infrared luminosities spanning a large range below the class of luminous infrared galaxies. We have found that:

- The mid-infrared emission of the normal galaxies in our sample is essentially contributed by a thermal continuum from very small grains (VSGs) longward of  $10\text{ }\mu\text{m}$  and the family of aromatic bands (UIBs) detected in a wide diversity of environments. It is the variation of the VSG component with respect to the UIBs that is responsible for  $F_{15}/F_7$  changes in our galaxies. From the comparison with observations of resolved Galactic regions, this can be related to an increase of the filling factor of star forming complexes by photoionized regions, hence a decrease of the contribution to the mid-infrared emission from neutral and molecular media.
- There is a dichotomy between spiral disks, where the integrated  $F_{15}/F_7$  color is close to 1 and shows little dispersion, and circumnuclear regions, where  $F_{15}/F_7$  ranges from disk-like to high values (up to 4). We have found no indication that destruction of UIB carriers occurs at the scale of circumnuclear regions, although it would be desirable to analyze infrared spectroscopic data of the most active galaxies, to elaborate on this.
- We confirm that barred spirals distinguish themselves from unbarred galaxies in the sense that they can reach higher  $F_{15}/F_7$  colors. This effect is however restricted to early morphological types, in agreement with previous IRAS-based studies (Hawarden et al. 1986; Huang et al. 1996). We show unambiguously that this emission excess arises in circumnuclear regions which can completely dominate the mid-infrared emission, although their size remains modest ( $D_{\text{CNR}}$  ranges between 2 and 26% of the optical diameter in the whole sample, with no clear dependency on Hubble type). Galaxies with a global color excess are all dominated by their central regions. This is a confirmation of predictions from hydrodynamical models (Athanasoula 1992; Friedli & Benz 1993), according to which a

barred perturbation, through tidal torques and shocks, induces substantial mass transfer towards circumnuclear regions. We observe the consequences of these gas flows, *i.e.* the intense star formation that they fuel.

- An important fact to mention is that only a fraction of early-type barred galaxies can be distinguished from unbarred galaxies in their infrared properties. Several interrelated parameters may explain this quiescence of many barred galaxies. With the present data we are unable to address this issue and thus only list possible explanations: a bar evolves on a much longer timescale than a starburst (Martinet & Friedli 1997) and the accretion rate by a bar is slow; the inward mass transfer is regulated by the depth of the potential well, the intensity of the shocks inside the bar, the star formation efficiency along the path of the inflowing gas before it reaches central regions (Martin & Friedli 1997), etc.

Although the presence of a bar can be an efficient means of triggering circumnuclear starbursts, the dust emission processes in central regions are the same in barred and unbarred galaxies. We have studied the properties of these central regions at the degree of detail accessible to our spatial resolution. Several physical properties were found to control the mid-infrared color  $F_{15}/F_7$ .

- The estimated molecular gas content inside the central regions ( $R_{\text{CNR}}$ ): as expected, the mid-infrared brightness at  $7\text{ }\mu\text{m}$  tends to rise with increasing mean gas density, which reflects the physical association of dust with molecular material. The  $F_{15}/F_7$  color is also correlated with the mean gas density. As a higher gas content allows more efficient star formation on relatively large scales, according to the Schmidt law and stability criteria or other empirical laws (Kennicutt 1998), this supports an interpretation of mid-infrared colors in terms of starburst intensity. A few galaxies, showing the most extreme  $F_{15}/F_7$  ratios, depart from the general trend. This could be interpreted as a transient evolutionary state of the starburst during which most of the gas has been consumed or dispersed, although a definite assessment of the effect requires better molecular line data.
- The age of the stellar populations heating dust: dust is sensitive to star formation on relatively long timescales, as can be expected from the fact that it can be heated by optical and near-UV photons. However, the strength of the VSG continuum is more sensitive to the radiation energy density and hardness than UIBs, and the results that we report here indicate that  $F_{15}/F_7$  excesses are linked to the weighted age of the exciting stellar populations. Mid-infrared colors are therefore influenced by the previous star formation history over at least 1 Gyr, and depend on the fraction of the ultraviolet radiation power contributed by young populations created in a contemporary starburst, with

respect to intermediate-age populations from already faded bursts.

*Acknowledgements.* We thank our referee, Louis Martinet, for his helpful remarks.

The ISOCAM data presented in this paper were analyzed using and adapting the CIA package, a joint development by the ESA Astrophysics Division and the ISOCAM Consortium (led by the PI C. Cesarsky, Direction des Sciences de la Matière, C.E.A., France).

## References

Aalto S., Booth R.S., Black J.H. & Johansson L.E.B., 1995, A&A 300, 369 (CO ref.: AB)

Aaronson M., Huchra J., Mould J.R. et al., 1982, ApJS 50, 241 (HI ref.: AH)

Aguerri J.A.L., 1999, A&A 351, 43

Allamandola L.J., Hudgins D.M. & Sandford S.A., 1999, ApJ 511, L115

Andreani P., Casoli F. & Gerin M., 1995, A&A 300, 43 (CO ref.: AC)

Appleton P.N., Foster P.A. & Davies R.D., 1986, MNRAS 221, 393 (HI ref.: AF)

Arsenault R., 1989, A&A 217, 66

Ashby M.L.N., Houck J.R. & Matthews K., 1995, ApJ 447, 545 (nuc. type ref.: A)

Athanassoula E., 1992, MNRAS 259, 345

Athanassoula E. & Martinet L., 1980, A&A 87, L10

Bajaja E., Wielebinski R., Reuter H.P., Harnett J.I. & Hummel E., 1995, A&AS 114, 147 (CO ref.: BW)

van den Bergh S., 1976, ApJ 206, 883

Bonatto C., Pastoriza M.G., Alloin D. & Bica E., 1998, A&A 334, 439

Borghesi A., Bussoletti E. & Colangeli L., 1987, ApJ 314, 422

Boselli A., Lequeux J., Sauvage M. et al., 1998, A&A 335, 53

Boselli A., Casoli F. & Lequeux J., 1995, A&AS 110, 521 (CO ref.: Bo)

Boulanger F., Abergel A., Bernard J.P., et al., 1998a, in "Star formation with the Infrared Space Observatory", J. Yun & R. Liseau Eds, ASP Conf. Series 132, 15

Boulanger F., Boissel P., Cesarsky D. & Ryter C., 1998b, A&A 339, 194

Boulanger F., Beichman C., Désert F.X. et al., 1988, ApJ 332, 328

Braine J., Combes F., Casoli F. et al., 1993, A&AS 97, 887 (CO ref.: Br)

Brooks K.J., Burton M.G., Rathborne J.M., Ashley M.C.B. & Storey J.W.V., 2000, MNRAS 319, 95

Buta R. & Block D.L., 2001, astro-ph/0010342, accepted for ApJ

Cayatte V., Kotanyi C., Balkowski C. & van Gorkom J.H., 1994, AJ 107, 1003

Cayatte V., van Gorkom J.H., Balkowski C. & Kotanyi C., 1990, AJ 100, 604

Cesarsky C.J., Abergel A., Agnese P. et al., 1996c, A&A 315, L32

Cesarsky D., Lequeux J., Abergel A. et al., 1996a, A&A 315, L309; 1996b, A&A 315, L305

Chamaraux P., Balkowski C. & Fontanelli P., 1986, A&A 165, 15 (HI ref.: C2)

Chamaraux P., Balkowski C. & Gérard E., 1980, A&A 83, 38 (HI ref.: C)

Claussen M.J. & Sahai R., 1992, AJ 103, 1134 (CO ref.: CS)

Cohen M., Allamandola L., Tielens A.G.G.M. et al., 1986, ApJ 302, 737

Combes F., Prugniel P., Rampazzo R. & Sulentic J.W., 1994, A&A 281, 725 (CO ref.: CP)

Combes F., Dupraz C., Casoli F. & Pagani L., 1988, A&A 203, L9 (CO ref.: CD)

Condon J.J., Frayer D.T. & Broderick J.J., 1991, AJ 101, 362

Contursi A., Lequeux J., Cesarsky D. et al., 2000, A&A 362, 310

Corwin H.G., de Vaucouleurs A. & de Vaucouleurs G., 1985, Southern Galaxy Catalogue

Dale D.A., Silbermann N.A., Helou G. et al., 2000, AJ 120, 583

Dale D.A., Helou G., Silbermann N.A. et al., 1999, AJ 118, 2055

Désert F.-X., Boulanger F. & Puget J.L., 1990, A&A 237, 215

Devereux N., 1987, ApJ 323, 91

Diaz A.I., Pagel B.E.J. & Wilson I.R.G., 1985, MNRAS 212, 737

Downes D., 1989, in "Evolution of Galaxies. Astronomical Observations", Les Houches Astrophysics School I, 351

Duley W.W. & Williams D.A., 1981, MNRAS 196, 269

Elfhag T., Booth R.S., Höglund B., Johansson L.E.B. & Sandqvist A., 1996, A&AS 115, 439 (CO ref.: E)

Eskridge P.B., Frogel J.A., Pogge R.W. et al., 2000, AJ 119, 536

Förster-Schreiber N.M., Laurent O., Sauvage M. et al., 2001, submitted to A&A

Friedli D. & Benz W., 1993, A&A 268, 65

Garcia A.M., 1993, A&AS 100, 47

García-Barreto J.A., Franco J., Carrillo R., Venegas S. & Escalante-Ramírez B., 1996, RevMexAA 32, 89

García-Barreto J.A., Downes D., Combes F. et al., 1991, A&A 252, 19 (CO ref.: GD)

Genzel R., Lutz D., Sturm E. et al., 1998, ApJ 498, 579

Gérin M., Nakai N. & Combes F., 1988, A&A 203, 44 (CO ref.: GN)

Giard M., Bernard J.P., Lacombe F., Normand P. & Rouan D., 1994, A&A 291, 239

Giovanardi C., Krumm N. & Salpeter E.E., 1983, AJ 88, 1719 (HI ref.: GK)

de Grijp M.H.K., Miley G.K. & Lub J., 1987, A&AS 70, 95

Guiderdoni B. & Rocca-Volmerange B., 1985, A&A 151, 108 (Hi ref.: GR)

Handa T., Nakai N., Sofue Y., Hayashi M. & Fujimoto M., 1990, PASJ 42, 1 (CO ref.: HN)

Hawarden T.G., Mountain C.M., Leggett S.K. & Puxley P.J., 1986, MNRAS 221, Short Com. 41

Haynes M.P., van Zee L., Hogg D.E., Roberts M.S. & Madalena R.J., 1998, AJ 115, 62 (Hi ref.: HZ)

Haynes M.P. & Giovanelli R., 1986, ApJ 306, 466 (Hi ref.: HG)

Heckman T.M., 1980, A&A 88, 365 (Research Note)

Helper T.T. & Blitz L., 1993, ApJ 419, 86 (CO ref.: HB)

Helou G., 1986, ApJ 311, L33

Helou G., Hoffman G.L. & Salpeter E.E., 1984, ApJS 55, 433 (Hi ref.: HH)

Ho L.C., Filippenko A.V. & Sargent W.L.W., 1997, ApJS 112, 315 (nuc. type ref.: H)

Horellou C., Casoli F. & Dupraz C., 1995, A&A 303, 361 (Hi ref.: HC)

Huang J.H., Gu Q.S., Su H.J. et al., 1996, A&A 313, 13

Huchtmeier W.K. & Seiradakis J.H., 1985, A&A 143, 216 (Hi ref.: HS)

Huchtmeier W.K. & Bohnenstengel H.D., 1981, A&A 100, 72 (Hi ref.: HB)

Huntley J.M., Sanders R.H. & Roberts W.W., 1978, ApJ 221, 521

Isobe T. & Feigelson E.D., 1992, ApJS 79, 197

Jörsäter S. & van Moorsel G.A., 1995, AJ 110, 2037 (Hi ref.: J)

Kamphuis J.J., Sijbring D. & van Albada T.S., 1996, A&AS 116, 15 (Hi ref.: Ka)

Keel W.C., 1984, ApJ 282, 75 (nuc. type ref.: K2)

Keel W.C., 1983, ApJS 52, 229 (nuc. type ref.: K)

Kenney J.D. & Young J.S., 1988, ApJS 66, 261 (CO ref.: KY)

Kennicutt R.C., 1998, ApJ 498, 541

Koopmann R.A. & Kenney J.D.P., 1998, ApJ 497, L75

Kotilainen J.K., Reunanen J., Laine S. & Ryder S.D., 2000, A&A 353, 834

Krügel E., Steppe H. & Chini R., 1990, A&A 229, 17 (CO ref.: KS)

Krumm N. & Salpeter E.E., 1980, AJ 85, 1312 (Hi ref.: Kr)

Kutner M.L. & Ulich B.L., 1981, ApJ 250, 341

Laurent O., Mirabel I.F., Charmandaris V. et al., 2000, A&A 359, 887

Léger A. & Puget J.L., 1984, A&A 137, L5

Lindblad P.O., Hjelm M., Högbom J. et al., 1996, A&AS 120, 403

Maia M.A.G., Pastoriza M.G., Bica E. & Dottori H., 1994, ApJS 93, 425 (Hi ref.: MP)

Maia M.A.G., da Costa L.N., Willmer C., Pellegrini P.S. & Ritè C., 1987, AJ 93, 546 (nuc. type ref.: MC)

Maiolino R., Ruiz M., Rieke G.H. & Papadopoulos P., 1997, ApJ 485, 552 (nuc. type ref.: M)

Maoz D., Koratkar A., Shields J.C. et al., 1998, AJ 116, 55

Martin P. & Friedli D., 1997, A&A 326, 449

Martin P., 1995, AJ 109, 2428

Martinet L. & Friedli D., 1997, A&A 323, 363

Mathewson D.S. & Ford V.L., 1996, ApJS 107, 97 (Hi ref.: MF)

Mauersberger R., Henkel C., Walsh W. & Schulz A., 1999, A&A 341, 256 (CO ref.: M)

McLeod K.K. & Rieke G.H., 1995, ApJ 441, 96

Mirabel I.F. & Sanders D.B., 1988, ApJ 335, 104 (Hi ref.: MS)

Moshir M., Copan G., Conrow T. et al., 1989, IRAS Faint Source Catalog

Mundell C.G. & Shone D.L., 1999, MNRAS 304, 475

Papoulias R., Conard J., Giuliano M., Kister J. & Mille G., 1989, A&A 217, 204

Pence W.D. & Blackman C.P., 1984, MNRAS 210, 547 (Hi ref.: P)

Phillips M.M. & Malin D.F., 1982, MNRAS 199, 905

Regan M.W., Vogel S.N. & Teuben P.J., 1997, ApJ 482, L143

Regan M.W., Teuben P.J. & Vogel S.N., 1996, AJ 112, 2549 (Hi ref.: RT)

Reynaud D. & Downes D., 1998, A&A 337, 671 (CO ref.: RD)

Rice W., Lonsdale C.J., Soifer B.T. et al., 1988, ApJS 68, 91

Richter O.G. & Huchtmeier W.K., 1987, A&AS 68, 427 (Hi ref.: RH)

Roche P.F., Aitken D.K. & Smith C.H., 1989, MNRAS 236, 485

Rogstad D.H., Shostak G.S. & Rots A.H., 1973, A&A 22, 111 (Hi ref.: RS)

Roth J., Mould J. & Staveley-Smith L., 1994, AJ 108, 851 (Hi ref.: RM)

Roussel H., Vigroux L., Sauvage M., 2001a, submitted to A&A (Paper II)

Roussel H., Vigroux L., Sauvage M., 2001b, accepted for A&A (Atlas)

Ryder S.D., Buta R.J., Toledo H. et al., 1996, ApJ 460, 665 (Hi ref.: RB)

Sage L.J. & Isbell D.W., 1991, A&A 247, 320 (CO ref.: SI)

Sakamoto K., Okumura S.K., Ishizuki S. & Scoville N.Z., 1999, ApJ 525, 691

Sakata A., Wada S., Onaka T. & Tokunaga A.T., 1987, ApJ 320, L63

Sancisi R., Allen R.J. & Sullivan W.T., 1979, A&A 78, 217 (Hi ref.: S)

Sandage A. & Bedke J., 1994, The Carnegie atlas of galaxies

Sanders D.B. & Mirabel I.F., 1996, ARA&A 34, 749

Sanders D.B., Scoville N.Z. & Soifer B.T., 1991, ApJ 370, 158 (CO ref.: SS)

Sandqvist A., Jörsäter S. & Lindblad P.O., 1995, A&A 295, 585 (CO ref.: SJ)

Seigar M.S. & James P.A., 1998, MNRAS 299, 672

Sellgren K., 1984, ApJ 277, 623

Sheth K., Regan M.W., Vogel S.N. & Teuben P.J., 2000, ApJ 532, 221 (CO ref.: SR)

Shioya Y., Tosaki T., Ohyama Y. et al., 1998, PASJ 50, 317 (CO ref.: ST)

Soifer B.T., Boehmer L., Neugebauer G. & Sanders D.B., 1989, AJ 98, 766

Spoon H.W.W., Koornneef J., Moorwood A.F.M., Lutz D. & Tielens A.G.G., 2000, A&A 357, 898

Strong A.W., Bloemen J.B.G.M., Dame T.M. et al., 1988, A&A 207, 1

Sturm E., Lutz D., Tran D. et al., 2000, A&A 358, 481

Taniguchi Y., Ohyama Y., Yamada T., Mouri H. & Yoshida M., 1996, ApJ 467, 215

Telesco C.M., Dressel L.L. & Wolstencroft R.D., 1993, ApJ 414, 120

Theureau G., Bottinelli L., Coudreau-Durand N. et al., 1998, A&AS 130, 333 (HI ref.: TB)

Thuan T.X. & Sauvage M., 1992, A&AS 92, 749

Tran D., 1998, PhD thesis, University of Paris XI

Tubbs A.D., 1982, ApJ 255, 458

Tully R.B., 1988, *Nearby Galaxies Catalog*, Cambridge University Press (HI ref.: T)

Uchida K.I., Sellgren K., Werner M.W. & Houdashelt M.L., 2000, ApJ 530, 817

de Vaucouleurs G., de Vaucouleurs A., Corwin H.G. et al., 1991, *Third Reference Cat. of Bright Galaxies (RC3)*

Veilleux S., Bland-Hawthorn J. & Cecil G., 1999, AJ 118, 2108

Veilleux S., Kim D.C., Sanders D.B., Mazzarella J.M. & Soifer B.T., 1995, ApJS 98, 171 (nuc. type ref.: VK)

Véron-Cetty M.P. & Véron P., 1986, A&AS 66, 335 (nuc. type ref.: V)

Vila-Vilaró B., Taniguchi Y. & Nakai N., 1998, AJ 116, 1553 (CO ref.: V)

Vorontsov-Velyaminov B.A. & Arkhipova V.P., 1968., *Morphological Catalog of Galaxies (part IV)*

Wiklind T., Henkel C. & Sage L.J., 1993, A&A 271, 71 (CO ref.: W1)

Wiklind T. & Henkel C., 1989, A&A 225, 1 (CO ref.: W2)

Whitworth A., 1979, MNRAS 186, 59

Young J.S., Xie S., Tacconi L. et al., 1995, ApJS 98, 219 (CO ref.: Y)

**Table 1.** General properties of sample galaxies. Virgo members are also named from the VCC catalog. Other galaxies belong to the field or loose groups, unless otherwise noted. Distances are from the NGC catalog of Tully (1988), taking into account the Virgo infall and assuming  $h_{100} = 0.75$ ; morphological types, asymptotic blue magnitudes  $m_{\text{BT}}$  and major diameters  $D_{25}$  at the isophote  $\mu_B = 25 \text{ mag arcsec}^{-2}$  are from the RC3 (de Vaucouleurs et al. 1991).

name	RA DEC (2000)	$D$ (Mpc)	morph. type	$m_{\text{BT}}$	$D_{25}$ ( $''$ )	HI def. <sup>a</sup>	$M_{\text{H}_2}$ ( $\log M_{\odot}$ )	$-(b)^b$ ( $''$ )	nuclear type	tidal <sup>c</sup>
N289	00 52 42–31 12.4	19.4	SBbc	11.72	5.13	-1.75 (P)			L/HII (V)	
N337	00 59 50–07 34.7	20.7	SBd	12.06	2.88	-0.82 (T)	8.05/7.65 (44) (E)		HII (V)	mbs
N613	01 34 18–29 25.0	17.5	SBbc	10.73	5.50	0.64 (MF)	9.20/9.04 (44) (E)		L/HII (V)	
N1022	02 38 33–06 40.7	18.5	SBa	12.09	2.40	0.98 (TB)	8.91/8.76 (44) (GD)		HII (A)	am
N1097	02 46 19–30 16.4	14.5	SBb	10.23	9.33	0.13 (MF)	9.33 (17) (GN)		L/Sy (V/M)	doa
N1365 †	03 33 37–36 08.3	16.9	SBb	10.32	11.22	0.22 (J)	9.69/9.68 (44) (SJ)		Sy1/2 (V/M)	
N1433 ‡	03 42 01–47 13.3	11.6	SBab	10.70	6.46	0.87 (RB)	8.36/8.24 (44) (BW)		L/Sy2 (V/M)	
N1530	04 23 29+75 17.8	36.6	SBb	12.25	4.57	-0.10 (RT)	9.65 (5.3) (RD)			
N1672 ‡	04 45 42–59 15.0	14.5	SBb	10.28	6.61	-1.24 (MP)	9.02/8.95 (44) (BW)		L/HII (V)	
N4027	11 59 30–19 16.1	25.6	SBdm	11.66	3.16	-0.62 (RH)			HII (V)	mbs
N4535 (V1555)	12 34 20+08 11.9	16.8	SABC	10.59	7.08	0.88 (GR)	8.73/8.72 (21) (*)		HII (V)	
N4691	12 48 14–03 20.0	22.5	SB0/a	11.66	2.82	0.24 (HS)	9.14 (21) (W1)		HII (K)	am
N4736 (M94)	12 50 54+41 07.2	4.3	SAab	8.99	11.22	0.77 (HS)	7.27/7.24 (16) (ST)		L (H)	
N5194 (M51)	13 29 53+47 11.8	7.7	SABC	8.96	11.22	-0.01 (AF)	8.95/8.99 (55) (HB)		Sy2 (H)	doa
N5236 (M83)	13 37 00–29 52.1	4.7	SABC	8.20	12.88	-2.40 (HB)	8.24 (16) (HN)		HII (V)	
N5383 (Mrk281)	13 57 05+41 50.7	37.8	SBb	12.05	3.16	0.36 (S)	9.53/9.39 (55) (SR)		HII (A)	
N5457 (M101)	14 03 13+54 20.9	5.4	SABcd	8.31	28.84	0.58 (HB)	7.97/7.82 (55) (SI)		HII (H)	doa
N6744	19 09 45–63 51.4	10.4	SABbc	9.14	19.95	-0.18 (MF)			L (V)	
N7552 §	23 16 11–42 35.0	19.5	SBab	11.25	3.39	-0.44 (T)	9.37/9.26 (44) (CS)		HII (V)	
<i>Virgo cluster sample:</i>										
N4178 (V66)	12 12 46+10 51.8	16.8	SBdm	11.90	5.13	0.33 (GR)			HII (H)	
N4192 (V92)	12 13 48+14 53.7	16.8	SABab	10.95	9.77	0.52 (GR)	8.58/8.43 (45) (KY)		L/HII (H)	
N4293 (V460)	12 21 13+18 23.0	17.0	SB0/a	11.26	5.62	1.23 (GR)	8.66/8.41 (45) (KY)		L (K)	
N4351 (V692)	12 24 02+12 12.4	16.8	SBab	13.03	2.00	0.41 (GR)				note
N4388 (V836) #	12 25 47+12 39.7	16.8	SBab/	11.76	5.62	1.84 (GR)	8.41/8.37 (16) (V)		Sy2 (K)	
N4394 (V857)	12 25 56+18 12.9	16.8	SBb	11.73	3.63	1.79 (GR)	8.12/7.89 (45) (KY)		L (K)	
N4413 (V912)	12 26 32+12 36.6	16.8	SBab	12.25	2.34	1.48 (GR)				
N4430 (V1002)	12 27 27+06 15.8	16.8	SBb	12.79	2.29	1.02 (HH)				doa
N4438 (V1043)	12 27 46+13 00.6	16.8	SA0/a	11.02	8.51	2.53 (GR)	8.99/8.88 (21) (CD)		L (K)	pc
N4450 (V1110)	12 28 29+17 05.1	16.8	SAab	10.90	5.25	1.78 (GR)	8.37/8.05 (44) (Bo)		L (K)	
N4491 (V1326)	12 30 57+11 29.0	16.8	SBa	13.50	1.70	>1.73 (GK)	7.73/7.35 (33) (Bo)			
N4498 (V1379)	12 31 40+16 51.2	16.8	SABd	12.79	2.95	1.68 (GR)				
N4506 (V1419)	12 32 11+13 25.3	16.8	SBa	13.63	1.62	>1.60 (HG)				
N4567 (V1673)	12 36 33+11 15.5	16.8	SABC	12.06	2.95	<1.04 (C)	8.32/7.97 (45) (KY)		HII (H)	
N4568 (V1676)	12 36 35+11 14.3	16.8	SABC	11.68	4.57		8.56/8.28 (33) (E)		HII (K)	
N4569 (V1690)	12 36 50+13 09.8	16.8	SABab	10.26	9.55	2.11 (GR)	8.98/8.77 (33) (Bo)		L/HII (H)	
N4579 (V1727)	12 37 44+11 49.2	16.8	SABb	10.48	5.89	1.94 (GR)	8.54/8.37 (33) (E)		L/Sy2 (H)	
N4580 (V1730)	12 37 48+05 22.2	16.8	SABA	11.83	2.09	1.92 (HH)				
N4633 (V1929)	12 42 37+14 21.4	16.8	SABdm	13.75	2.14	0.40 (HH)				
N4634 (V1932)	12 42 40+14 17.8	16.8	SBcd/	13.16	2.57	1.05 (HH)				
N4647 (V1972)	12 43 32+11 34.9	16.8	SABC	11.94	2.88	1.82 (GR)	8.11/7.79 (45) (KY)		HII (K)	
N4654 (V1987)	12 43 57+13 07.6	16.8	SABcd	11.10	4.90	0.16 (GR)	8.32/8.12 (21) (Br)		HII (V)	doa
N4689 (V2058)	12 47 46+13 45.8	16.8	SABC	11.60	4.27	1.44 (GR)			HII (K)	

**Table 1.** continued. The last column indicates the name of the observation project: *S* for *Sf-glx* or *Hi-Q-gal* for IC 1953 (PI: G. Helou), and *I* for *Irgal* (PI: T. Onaka).

name	RA DEC (2000)	<i>D</i> (Mpc)	morph. type	<i>m<sub>BT</sub></i>	<i>D<sub>25</sub></i> ( $''$ )	HI def. <sup>a</sup>	<i>M<sub>H2</sub></i> (log M $_{\odot}$ )	– ( <i>b</i> ) <sup>b</sup> – ( $''$ )	nuclear type	tidal <sup>c</sup> int.
<i>Supplementary galaxies:</i>										
N986	02 33 34–39 02.6	23.2	SBab	11.64	3.89	0.47 (RM)	9.48/9.39 (44) (E)	HII (V)	<i>S</i>	
N1326 †	03 23 56–36 27.9	16.9	SB0+	11.37	3.89	-0.18 (HC)	8.43/8.33 (44) (W2)	L (MC)	<i>S</i>	
N1385	03 37 28–24 30.1	17.5	SBcd	11.45	3.39	-0.14 (AH)	8.31/7.90 (44) (AC)	HII (V)	mbs <i>S</i>	
N3583	11 14 11+48 19.1	34.0	SBb	11.90	2.82	-0.31 (T)	9.45/9.09 (55) (SS)	HII (H)	<i>S</i>	
N3620 <sup>d</sup>	11 16 04–76 12.9	23.7	SBab		2.75	0.60 (RM)	9.61/9.44 (44) (E)		<i>S</i>	
N3683	11 27 32+56 52.6	28.4	SBc	13.15	1.86	-1.46 (Ka)			<i>S</i>	
N3705	11 30 07+09 16.6	17.0	SABab	11.86	4.90	-0.28 (HZ)		L/HII (H)	<i>S</i>	
N3885	11 46 47–27 55.4	27.8	SA0/a	11.89	2.40	-1.08 (C2)			<i>S</i>	
N4041	12 02 12+62 08.2	22.7	SAbc	11.88	2.69	-0.82 (T)	8.86/8.80 (33) (E)	HII (H)	<i>I</i>	
N4102 ‡	12 06 23+52 42.7	17.0	SABB	11.99	3.02	0.53 (T)	9.13/9.08 (21) (M)	HII (H)	<i>S</i>	
N4519 (V1508)	12 33 30+08 39.3	16.8	SBd	12.34	3.16	-0.32 (GR)	7.63/7.29 (45) (Y)		<i>S</i>	
N4713	12 49 58+05 18.7	17.9	SABd	12.19	2.69	-0.82 (HZ)		L/HII (H)	<i>S</i>	
N5430 (Mrk799) <sup>d</sup>	14 00 46+59 19.7	40.4	SBb	12.72	2.19	0.81 (TB)	9.52/9.43 (21) (KS)	HII (K2)	<i>I</i>	
N5786 <sup>d</sup>	14 58 57–42 00.8	39.7	SBbc	12.17	2.34	-0.96 (RM)			<i>S</i>	
N5937 <sup>d</sup>	15 30 46–02 49.8	36.8	SABb	13.11	1.86	0.60 (TB)		L/HII (A)	<i>I</i>	
N5962	15 36 32+16 36.5	31.8	SAc	11.98	2.95	0.57 (Kr)		HII (V)	<i>S</i>	
N6156 <sup>d</sup>	16 34 52–60 37.1	42.9	SABc	12.30	1.58				<i>I</i>	
N6753 <sup>d</sup>	19 11 23–57 02.9	42.4	SAb	11.97	2.45				<i>S</i>	
N6824 <sup>d</sup>	19 43 41+56 06.6	44.5	SAb	13.00	1.70	0.80 (K)			<i>I</i>	
N6946	20 34 52+60 09.2	5.5	SABcd	9.61	11.48	-1.22 (RS)		HII (H)	<i>S</i>	
N7218	22 10 12–16 39.6	22.0	SBcd	12.70	2.51	-0.70 (T)			<i>S</i>	
N7418	22 56 36–37 01.8	17.8	SABcd	11.65	3.55	0.28 (T)			<i>S</i>	
N7771 (Mrk9006) <sup>d</sup>	23 51 25+20 06.7	57.4	SBa	13.08	2.51	0.28 (MS)	9.86/9.58 (45) (Y)	HII (VK)	<i>S</i>	
IC1953	03 33 42–21 28.8	22.1	SBd	12.24	2.75	1.34 (T)	8.46/8.20 (44) (CP)		<i>S</i>	
IC2554	10 08 50–67 01.8	16.7	SBbc	12.51	3.09	-0.35 (RC3)	8.65/8.34 (44) (AB)		doa <i>I</i>	
IC5325	23 28 43–41 20.0	18.1	SABbc	11.83	2.75	0.79 (T)			<i>S</i>	
ESO317-G023 <sup>d</sup>	10 24 43–39 18.4	32.8	SBa	13.93	1.91				<i>S</i>	

<sup>a</sup> The HI deficiency according to the definition and reference values of Guiderdoni & Rocca (1985). It is normalized by the dispersion in the field sample. Diameters are taken from the RC2 for consistency, and HI fluxes from the indicated references. NGC 4567/68 are unresolved in HI. When  $D_{\text{HI}}/D_{\text{opt}} \leq 1$ . and  $Def \geq 0.5$  in Cayatte et al. (1994), it corresponds to  $def > 1.2$  here.

<sup>b</sup> The given range represents the effect of varying the scale length of the CO distribution from once to twice that of infrared circumnuclear regions (see text). *b* is the beam HPBW of the observations used. (\*) NGC 4535 was observed by A. Bosma, D. Reynaud and H. Roussel at the IRAM 30 m telescope.

<sup>c</sup> Signs of tidal interaction. “doa”: asymmetrical distortion of outer arms. “mbs”: magellanic barred spiral. “am”: amorphous. “pc”: past collision. “note”: On DSS images, the brightness peak is displaced by  $\approx 10''$  ENE from the center of the regular outer isophotes and the NW outer disk seems depressed in stars and gas.

† members of the Fornax cluster of galaxies. ‡ members of the Dorado group of galaxies. § member of the Grus quartet with NGC 7582/90/99. ¶ member of the spiral-rich Ursa Major cluster.

# classified SA in the RC3, here considered a SB after the morphological arguments of Phillips & Malin (1982) and McLeod & Rieke (1995), and the recent kinematic analysis of Veilleux et al. (1999).

<sup>d</sup> The distances of ESO 317-G023, NGC 6753 and 6156 were assumed to be those of the galaxy groups LGG 199, LGG 426 and LGG 407 (Garcia 1993); those of NGC 5786 and 7771 were estimated from the HI redshift, that of NGC 3620 from the CO redshift and those of NGC 5430, 5937 and 6824 from the optical redshift (with  $h_{100} = 0.75$ ).

**Table 2.** Photometric results at 15 and 7  $\mu\text{m}$ , obtained as described in the Atlas (total fluxes, diameter aperture used for central regions, fluxes inside this aperture and background levels). We warn the reader that the uncertainties can only be taken as order-of-magnitude values (see the text), especially for galaxies of the third subsample belonging to the *Sf\_glx* project, with a very low number of exposures per sky position. Galaxies with no reported central fluxes have no identifiable central concentration: the radial surface brightness profile is consistent with a disk alone at our angular resolution (NGC 4580 rather shows a smooth central plateau and NGC 4634 is seen edge-on). For NGC 7552, we used only the maps with a 3'' pixel size, because those at 6'' are strongly saturated in both filters; for the other galaxies mapped with both pixel sizes, we used the 6'' sampling because of the higher signal to noise ratio and the more reasonable field of view.

name	$F_{15\text{ tot}}$ (mJy) <sup>a</sup>	$F_{7\text{ tot}}$ (mJy) <sup>a</sup>	$D_{\text{CNR}}$ ('')	$F_{15\text{ CNR}}$ (mJy) <sup>a</sup>	$F_{7\text{ CNR}}$ (mJy) <sup>a</sup>	$b_{15}$ ( $\mu\text{Jy arcsec}^{-2}$ )	$b_7$ ( $\mu\text{Jy arcsec}^{-2}$ )
N289	327.8 $\pm$ 25.6	342.9 $\pm$ 14.7	12.9	1.21	68.5 $\pm$ 4.2	37.5 $\pm$ 1.8	588. $\pm$ 6.
N337	297.9 $\pm$ 24.0	336.1 $\pm$ 17.9	11.3	1.13	31.8 $\pm$ 2.2	28.5 $\pm$ 1.1	679. $\pm$ 6.
N613	1566.5 $\pm$ 104.0	1473.3 $\pm$ 71.4	19.1	1.62	557.1 $\pm$ 47.8	353.4 $\pm$ 31.3	534. $\pm$ 6.
N1022	802.3 $\pm$ 86.4	444.4 $\pm$ 45.3	15.0	1.34	748.9 $\pm$ 81.2	350.8 $\pm$ 39.2	744. $\pm$ 9.
N1097	2269.2 $\pm$ 167.4	2128.6 $\pm$ 125.4	45.6	3.21	1730.3 $\pm$ 92.6	1285.1 $\pm$ 65.2	416. $\pm$ 6.
N1365	4436.7 $\pm$ 764.5	3691.9 $\pm$ 616.6	42.6	3.49	3163.2 $\pm$ 420.2	2019.0 $\pm$ 301.2	370. $\pm$ 4.
N1433	355.3 $\pm$ 41.0	381.3 $\pm$ 33.8	31.1	1.75	117.2 $\pm$ 3.3	105.3 $\pm$ 2.4	352. $\pm$ 5.
N1530	606.1 $\pm$ 39.2	573.9 $\pm$ 39.1	27.7	4.92	267.6 $\pm$ 10.2	217.0 $\pm$ 9.8	345. $\pm$ 5.
N1672	2020.5 $\pm$ 123.0	1985.0 $\pm$ 129.2	32.4	2.28	1179.8 $\pm$ 74.7	956.7 $\pm$ 69.8	340. $\pm$ 5.
N4027	676.7 $\pm$ 95.5	775.8 $\pm$ 68.2	10.5	1.30	31.7 $\pm$ 6.4	32.4 $\pm$ 4.3	900. $\pm$ 4.
N4535	1127.9 $\pm$ 181.4	1136.6 $\pm$ 68.9	23.2	1.89	153.4 $\pm$ 15.8	111.8 $\pm$ 14.2	1043. $\pm$ 5.
N4691	795.9 $\pm$ 185.6	613.5 $\pm$ 83.1	44.9	4.90	730.5 $\pm$ 81.4	510.9 $\pm$ 53.5	1374. $\pm$ 5.
N4736 (-)	4204.5 $\pm$ 240.6	3913.9 $\pm$ 225.8	21.6	0.45	566.2 $\pm$ 39.2	540.6 $\pm$ 49.0	473. $\pm$ 10.
N5194	8003.2 $\pm$ 493.5	8598.7 $\pm$ 552.1	88.9	3.32	2032.7 $\pm$ 33.4	1869.3 $\pm$ 40.5	412. $\pm$ 10.
N5236 #	20098.4 $\pm$ 803.7	18474.9 $\pm$ 899.7	36.8	0.84	3473.9 $\pm$ 200.2	2656.4 $\pm$ 203.3	1096. $\pm$ 5.
N5383	332.6 $\pm$ 61.9	350.2 $\pm$ 62.1	32.1	5.89	185.8 $\pm$ 20.1	171.3 $\pm$ 20.9	394. $\pm$ 3.
N5457	5424.3 $\pm$ 322.0	6034.0 $\pm$ 116.7	35.2	0.92	129.0 $\pm$ 9.2	114.5 $\pm$ 4.7	361. $\pm$ 2.
N6744 (-)	1497.4 $\pm$ 125.7	2419.4 $\pm$ 52.3	32.4	1.64	26.6 $\pm$ 5.6	50.3 $\pm$ 2.1	485. $\pm$ 6.
N7552 #	2767.6 $\pm$ 193.7	1826.2 $\pm$ 168.5	21.3	2.01	2292.1 $\pm$ 153.3	1251.8 $\pm$ 137.4	565. $\pm$ 7.
<i>Virgo cluster sample:</i>							
N4178	181.5 $\pm$ 48.0	228.5 $\pm$ 24.6	23.8	1.94	34.6 $\pm$ 4.7	33.4 $\pm$ 2.1	1051. $\pm$ 3.
N4192	630.0 $\pm$ 99.6	900.8 $\pm$ 68.3	29.3	2.39	132.3 $\pm$ 16.4	120.0 $\pm$ 23.8	638. $\pm$ 3.
N4293 (+)	188.6 $\pm$ 42.8	159.5 $\pm$ 25.3	13.9	1.15	128.0 $\pm$ 34.9	50.2 $\pm$ 12.4	916. $\pm$ 3.
N4351	45.6 $\pm$ 26.3	52.6 $\pm$ 8.7	16.8	1.37	14.3 $\pm$ 4.7	14.8 $\pm$ 1.0	998. $\pm$ 3.
N4388 #	1008.2 $\pm$ 244.0	499.4 $\pm$ 77.8	20.8	1.70	763.3 $\pm$ 244.9	224.7 $\pm$ 66.6	994. $\pm$ 3.
N4394	139.0 $\pm$ 41.0	161.2 $\pm$ 19.1	18.6	1.52	19.7 $\pm$ 2.9	21.6 $\pm$ 3.2	905. $\pm$ 3.
N4413	93.0 $\pm$ 31.4	89.3 $\pm$ 11.0	14.2	1.16	27.0 $\pm$ 4.0	22.4 $\pm$ 2.6	992. $\pm$ 3.
N4430	98.0 $\pm$ 23.5	132.5 $\pm$ 13.9					986. $\pm$ 4.
N4438 (+)	209.1 $\pm$ 34.7	231.9 $\pm$ 26.9	21.0	1.71	123.8 $\pm$ 22.7	103.3 $\pm$ 10.0	906. $\pm$ 3.
N4450 (+)	169.7 $\pm$ 42.5	185.1 $\pm$ 14.6	17.3	1.41	28.5 $\pm$ 4.5	28.1 $\pm$ 2.9	879. $\pm$ 3.
N4491	81.1 $\pm$ 25.2	30.5 $\pm$ 7.6	10.4	0.85	73.4 $\pm$ 21.4	18.3 $\pm$ 4.0	1052. $\pm$ 3.
N4498	94.6 $\pm$ 19.2	112.9 $\pm$ 11.8	14.7	1.20	11.6 $\pm$ 2.2	11.2 $\pm$ 1.0	876. $\pm$ 3.
N4506	12.7 $\pm$ 5.2	21.1 $\pm$ 9.8	13.0	1.06	7.5 $\pm$ 3.4	7.6 $\pm$ 0.9	895. $\pm$ 3.
N4567 †	293.4 $\pm$ 15.5	317.9 $\pm$ 16.4	18.0	1.47	50.0 $\pm$ 5.7	41.3 $\pm$ 2.3	979. $\pm$ 3.
N4568 †	1099.0 $\pm$ 127.6	1074.7 $\pm$ 64.8	17.5	1.42	230.2 $\pm$ 47.5	172.2 $\pm$ 23.0	979. $\pm$ 3.
N4569	939.3 $\pm$ 125.1	843.5 $\pm$ 54.1	21.3	1.73	289.2 $\pm$ 88.1	144.1 $\pm$ 23.4	871. $\pm$ 3.
N4579	619.2 $\pm$ 85.1	672.5 $\pm$ 37.5	26.4	2.15	152.2 $\pm$ 36.4	96.4 $\pm$ 9.7	973. $\pm$ 3.
N4580	103.9 $\pm$ 24.2	102.6 $\pm$ 7.7					1006. $\pm$ 3.
N4633	30.0 $\pm$ 9.5	30.3 $\pm$ 9.1					830. $\pm$ 3.
N4634	258.2 $\pm$ 40.7	278.3 $\pm$ 35.0					830. $\pm$ 3.
N4647	472.3 $\pm$ 32.0	474.3 $\pm$ 17.2	16.9	1.38	61.1 $\pm$ 6.9	52.8 $\pm$ 2.7	849. $\pm$ 3.
N4654	1018.6 $\pm$ 78.4	1049.4 $\pm$ 42.9	15.5	1.26	92.5 $\pm$ 25.9	82.9 $\pm$ 11.2	823. $\pm$ 3.
N4689	329.7 $\pm$ 37.4	340.9 $\pm$ 16.3					796. $\pm$ 3.

**Table 2.** continued.

name	$F_{15\text{ tot}}$ (mJy) <sup>a</sup>	$F_{7\text{ tot}}$	$D_{\text{CNR}}$ (")	$F_{15\text{ CNR}}$ (mJy) <sup>a</sup>	$F_{7\text{ CNR}}$	$b_{15}$ ( $\mu\text{Jy arcsec}^{-2}$ )	$b_7$
<i>Supplementary galaxies:</i>							
N986	$1050.0 \pm 79.0$	$801.5 \pm 12.1$	22.9	2.57	$657.0 \pm 67.1$	$316.1 \pm 11.5$	$372 \pm 4$
N1326	$287.8 \pm 58.8$	$284.9 \pm 18.8$	33.1	2.71	$258.4 \pm 35.6$	$212.3 \pm 16.1$	$353 \pm 4$
N1385	$782.3 \pm 62.7$	$815.7 \pm 27.1$	12.9	1.10	$79.9 \pm 7.2$	$68.5 \pm 4.6$	$385 \pm 4$
N3583	$448.4 \pm 52.5$	$425.6 \pm 19.1$	14.0	2.31	$87.2 \pm 4.2$	$70.0 \pm 5.0$	$517 \pm 5$
N3620 #	$1199.8 \pm 408.6$	$723.1 \pm 89.2$	30.2	3.47	$1087.2 \pm 408.3$	$537.2 \pm 74.7$	$386 \pm 4$
N3683	$755.5 \pm 71.3$	$791.1 \pm 57.4$					$452 \pm 5$
N3705	$307.4 \pm 73.6$	$348.2 \pm 32.6$	14.1	1.16	$28.6 \pm 1.8$	$28.9 \pm 2.1$	$686 \pm 6$
N3885	$396.0 \pm 16.0$	$342.9 \pm 10.2$	30.7	4.14	$363.9 \pm 8.9$	$293.0 \pm 9.8$	$738 \pm 5$
N4041	$751.9 \pm 128.1$	$792.8 \pm 164.5$	36.4	4.01	$482.8 \pm 69.5$	$476.7 \pm 123.7$	$428 \pm 6$
N4102 #	$1712.9 \pm 561.0$	$808.8 \pm 125.9$	24.3	2.00	$1419.2 \pm 570.7$	$462.3 \pm 113.7$	$443 \pm 5$
N4519	$233.8 \pm 67.6$	$177.8 \pm 18.3$	11.2	0.91	$85.3 \pm 24.3$	$20.3 \pm 0.8$	$1050 \pm 6$
N4713	$209.4 \pm 55.7$	$223.6 \pm 13.3$					$845 \pm 6$
N5430	$530.1 \pm 136.1$	$364.8 \pm 153.7$	20.7	4.05	$273.0 \pm 80.3$	$152.5 \pm 106.9$	$375 \pm 5$
N5786	$380.2 \pm 81.6$	$345.8 \pm 25.5$	19.3	3.72	$120.1 \pm 15.5$	$85.7 \pm 5.4$	$823 \pm 7$
N5937	$616.1 \pm 128.9$	$562.3 \pm 94.6$	7.4	1.33	$157.7 \pm 90.1$	$85.2 \pm 29.1$	$1140 \pm 8$
N5962	$508.8 \pm 37.2$	$485.5 \pm 17.0$					$499 \pm 5$
N6156	$827.0 \pm 149.2$	$697.9 \pm 118.0$					$457 \pm 6$
N6753	$646.8 \pm 60.1$	$586.4 \pm 16.9$	32.3	6.64	$247.8 \pm 7.3$	$218.7 \pm 3.1$	$466 \pm 5$
N6824	$394.6 \pm 98.1$	$408.3 \pm 101.3$	9.8	2.11	$81.5 \pm 30.3$	$74.4 \pm 23.6$	$335 \pm 5$
N6946 #	$10651.6 \pm 1767.2$	$11648.8 \pm 678.6$	30.2	0.81	$1730.4 \pm 747.0$	$970.6 \pm 277.5$	$424 \pm 5$
N7218	$273.5 \pm 54.1$	$260.6 \pm 12.8$					$1013 \pm 7$
N7418	$455.5 \pm 113.3$	$469.8 \pm 32.9$	17.9	1.55	$38.6 \pm 3.1$	$31.1 \pm 1.2$	$640 \pm 5$
N7771	$615.2 \pm 116.6$	$526.8 \pm 57.4$	19.4	5.41	$323.8 \pm 76.1$	$247.1 \pm 33.9$	$869 \pm 6$
I1953	$222.9 \pm 37.0$	$186.2 \pm 13.7$	14.3	1.53	$116.2 \pm 23.1$	$34.4 \pm 2.8$	$429 \pm 3$
I2554	$887.6 \pm 345.2$	$733.5 \pm 242.6$	17.9	1.45	$503.9 \pm 369.7$	$264.0 \pm 183.4$	$376 \pm 5$
I5325	$373.9 \pm 42.2$	$364.6 \pm 17.4$					$537 \pm 5$
ESO317	$287.2 \pm 59.2$	$239.8 \pm 38.4$	19.9	3.17	$222.2 \pm 32.4$	$162.1 \pm 20.7$	$519 \pm 5$
							$112 \pm 3$

<sup>a</sup> The conversion from flux densities to fluxes is:  $F(\text{W m}^{-2}) = 10^{-14} F_{\lambda}(\text{Jy}) \times \Delta_{\nu}(\lambda)(\text{THz})$ , with the filter widths  $\Delta_{\nu}(15) = 6.75 \text{ THz}$  and  $\Delta_{\nu}(7) = 16.18 \text{ THz}$ .

# : nucleus saturated (for NGC 5236: both at 15 and 7  $\mu\text{m}$ , but more severely at 15  $\mu\text{m}$  since the same gain and integration time were used for both filters and since  $F_{15}/F_7$  is above 1 in electronic units; for NGC 7552: slightly at 15  $\mu\text{m}$ , but not at 7  $\mu\text{m}$ ; for the central pixel of NGC 4388: at 15  $\mu\text{m}$ , but not at 7  $\mu\text{m}$ ; for NGC 3620: at 7  $\mu\text{m}$  but not at 15  $\mu\text{m}$ , which is possible because the integration time was respectively 5 s and 2 s; for NGC 4102 and 6946: both at 7 and 15  $\mu\text{m}$ , but more severely at 7  $\mu\text{m}$ , with the same configuration as NGC 3620). Thus,  $F_{15}/F_7$  colors in central regions are respectively lower limits for NGC 5236, 7552 and 4388 and upper limits for NGC 3620, 4102 and 6946.

(-) : The field of view is too small to allow a precise determination of the background level and total fluxes are lower limits. The error bars are only formal. The comparison of our measurements with those of Rice et al. (1988) at 12  $\mu\text{m}$ , inside the IRAS band 8–15  $\mu\text{m}$  which overlaps with our 5–8.5  $\mu\text{m}$  and 12–18  $\mu\text{m}$  bands, indicates that we miss of the order of 15% of total fluxes for NGC 4736 and between 15 and 45% for NGC 6744, provided IRAS fluxes are not overestimated as this is often the case for co-added observations.

(+) : From their spectral energy distributions shown by Boselli et al. (1998), these galaxies probably have a non-negligible contribution from the Rayleigh-Jeans tail of cold stars to their 7  $\mu\text{m}$  emission. We did not attempt to remove this contribution, because it would require a careful modelling of stellar populations.

† : The disks of these galaxies slightly overlap in projection. We attempted to separate them by the means of a mask defined visually, but the disk fluxes are much more uncertain than estimated.